Geomechanics for Energy and the Environment 29 (2022) 100275

Contents lists available at ScienceDirect

Geomechanics for Energy and the Environment

journal homepage: www.elsevier.com/locate/gete

Experimental analysis of a thermoactive underground railway station

Jacopo Zannin [a,*], Alessio Ferrari [a,b], Tohid Kazerani [c], Azad Koliji [c], Lyesse Laloui [a]

[a] Swiss Federal Institute of Technology in Lausanne, EPFL, Laboratory of Soil Mechanics, EPFL-ENAC-IIC-LMS, Station 18, 1015 Lausanne, Switzerland
[b] Università degli Studi di Palermo, Engineering Department, Italy
[c] BG Consulting Engineers, Av. de Cour 61, 1007 Lausanne, Switzerland

ARTICLE INFO

Article history:
Received 27 May 2021
Received in revised form 1 September 2021
Accepted 4 October 2021
Available online 19 October 2021

Editors-in-Chief:
Professor Lyesse Laloui and Professor Tomasz Hueckel

Keywords:
Energy geostructures
Energy walls
Underground infrastructures
Thermomechanical behavior
Soil–structure interaction
Thermal response test

ABSTRACT

Little is known about the real energy potential of thermoactive underground infrastructures, such as railway stations, that can act as a heating/cooling provider for the built environment. This study presents the results of thermomechanical full-scale in situ testing and numerical analysis of a thermoactive underground train station. The thermal performance and related geostructural impact of a portion of the new underground energy infrastructure (UEI) installed at the Lancy-Bachet train station in Geneva (Switzerland) are analyzed. Heating and cooling tests simulating real operative geothermal conditions are considered. Particular attention is given to (*i*) the monitored wall–tunnel hydrothermal interactions, (*ii*) the thermal response of the UEI to heating/cooling thermal inputs and (*iii*) the thermomechanical behavior of the energy geostructure. Among the main results of this study, it is shown how the hydrothermal tunnel behavior considerably varies on a seasonal basis, while the train circulation completely drives the airflow in the tunnel. The UEI shows a strong heat storage potential due to the main conductive heat transfers between the geostructure and soil, while lower heat fluxes are detected at the wall–tunnel interface. The extraction potential is of lower magnitude with respect to storage because of the limited range of operative fluid temperatures and of the concurrent action of temperature variations at the tunnel boundaries affecting the materials within the UEI. Preliminary guidelines for the thermal response test execution on underground thermoactive infrastructures are also reported. The monitored thermomechanical behavior suggests different wall behaviors in the vertical and longitudinal directions. Low-magnitude strains are recorded, while the mechanical capacity of the existing geostructure can satisfactorily sustain concurrent thermomechanical actions.

© 2021 The Author(s). Published by Elsevier Ltd. This is an open access article under the CC BY-NC-ND license (http://creativecommons.org/licenses/by-nc-nd/4.0/).

1. Introduction

Thermal activation of shallow underground infrastructures may represent an important source of thermal energy for the built environment. In recent years, an increasing number of installations using shallow geothermal technologies (e.g., energy geostructures, EGs) have been recorded around the world.[1] In EGs, the dual role of geostructures is enhanced: they involve structural support and a geothermal heat exchanger role. The EG has proven to be an efficient renewable solution for heating/cooling of the built environment.[2] This technology has been approached by the scientific community and shows a promising future.[1,3] Examples of underground energy infrastructures (UEIs) include but are not limited to underground circular and cut-and-cover tunnels used for transportation and/or services, underground train stations, trenches, and sewers. Within UEIs, heat exchangers (i.e., plastic pipes) can be secured to the steel cage of the reinforced concrete geostructure, and they exchange heat with the surrounding materials by circulating a fluid.

Knowledge on UEIs lacks feedback from real monitored installations, whose experience could be crucial to fully understand the performance of ongoing multiphysical processes and to allow design optimization strategies and guidelines for future installations. In this regard, few field experiments are available in the literature. Attempts to understand the thermal behavior highlighted that the heat exchanger (HE) configuration plays a crucial role and that wall–tunnel thermal interactions could be non-negligible.[4–6] Different thermal performances for energy walls (EWs) and slabs were recorded, with the former outperforming the latter for the particular case study presented in Refs. 7, 8 As regard to the thermomechanical behavior, low-magnitude thermally induced deformations were registered at the Lainzer U2 line in Vienna.[9] The complex multiphysical aspects involved within UEI operations make it difficult to thoroughly understand and describe their thermal, hydraulic and mechanical behavior.[10] From an energy performance perspective, the thermal response test (i.e., TRT) execution for UEI is challenging, as reported by Refs. 11, 12. Despite the interesting knowledge acquired from

* Corresponding author.
E-mail address: jacopo.zannin@gmail.com (J. Zannin).

https://doi.org/10.1016/j.gete.2021.100275
2352-3808/© 2021 The Author(s). Published by Elsevier Ltd. This is an open access article under the CC BY-NC-ND license (http://creativecommons.org/licenses/by-nc-nd/4.0/).

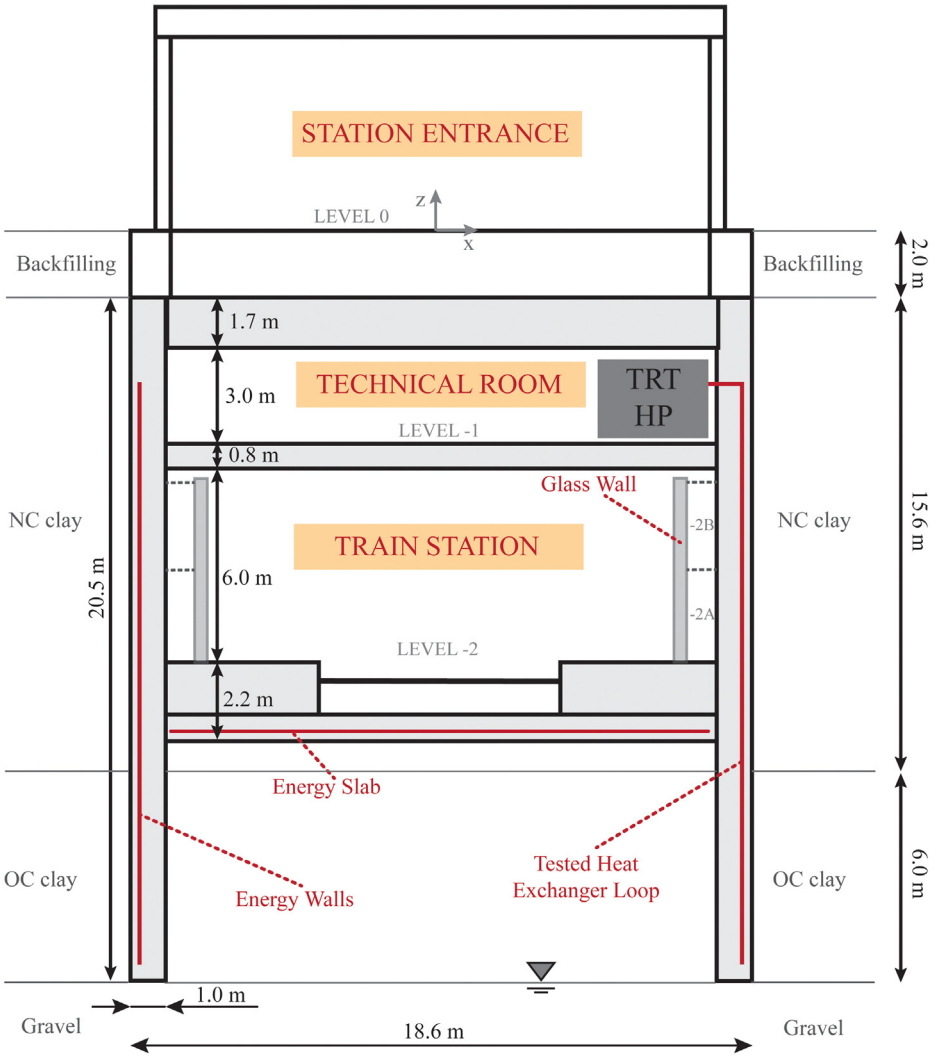

Fig. 1. Cross section of the Lancy-Bachet underground train station with an indication of the heat exchanger locations.

these studies, no guidelines for TRT execution on geostructures facing air interfaces are available.

Exploiting a new UEI installation in Geneva (Switzerland), thermo-hydro-mechanical (THM) in situ tests were possible. This represented a unique opportunity to further investigate fundamental aspects linked to the multiphysical behavior of UEIs, as well as to develop preliminary guidelines for successful THM in situ test execution. The UEI was tested under real operational conditions, which means that it was subjected to heating/cooling geothermal operations along with mechanical and environmental actions. The study was conducted with the following objectives: (*i*) to investigate the real THM behavior of the UEI through a series of full-scale in situ experimental tests upon heating and cooling thermal inputs; (*ii*) to understand the rationale behind fundamental THM aspects linked to thermal activation of underground infrastructures; and (*iii*) to propose preliminary guidelines for in situ test execution.

In this paper, after a description of the tested site and experimental setup, hydrothermal aspects are approached, followed by thermomechanical ones. Experimental results are presented, discussed and interpreted with the help of numerical simulations validated against experimental results, which allow us to have a complete picture of the THM aspects involved in UEI operation. Concluding remarks on the geothermal exploitation of the tested UEI are finally reported.

2. The experimental campaign

In this section, the implemented energy geostructure is outlined, and then the experimental campaign and setup is described.

2.1. The tested energy geostructure

The tested site is located in the southwestern part of Geneva, Switzerland. A new railway line that connects Geneva to Annemasse (France) was recently constructed. One of the train stations, Lancy-Bachet, is equipped with EWs and energy slabs presenting a total thermoactive surface of approximately 5000 m^2. In plain view, the train station represents the entrance point of the underground tunnel portion, going toward Annemasse. A vertical cross section is depicted in Fig. 1, while photos of the site are shown in Fig. 2. The accessible underground space consists of two levels (Fig. 1), where the bottom level (level -2) is the railway level. At level -2, an architectural element composed of a glass wall sustained by a steel structure is installed at a distance of 1 m from the concrete walls (Fig. 1 and Fig. 2(a)). The space between these two walls is partly separated into two regions by a steel grid, hereafter named levels -2 A and -2B (Fig. 1 and Fig. 2(a), respectively). This architectural choice will affect the airflow near the wall, a topic that will be further expanded later in this paper.

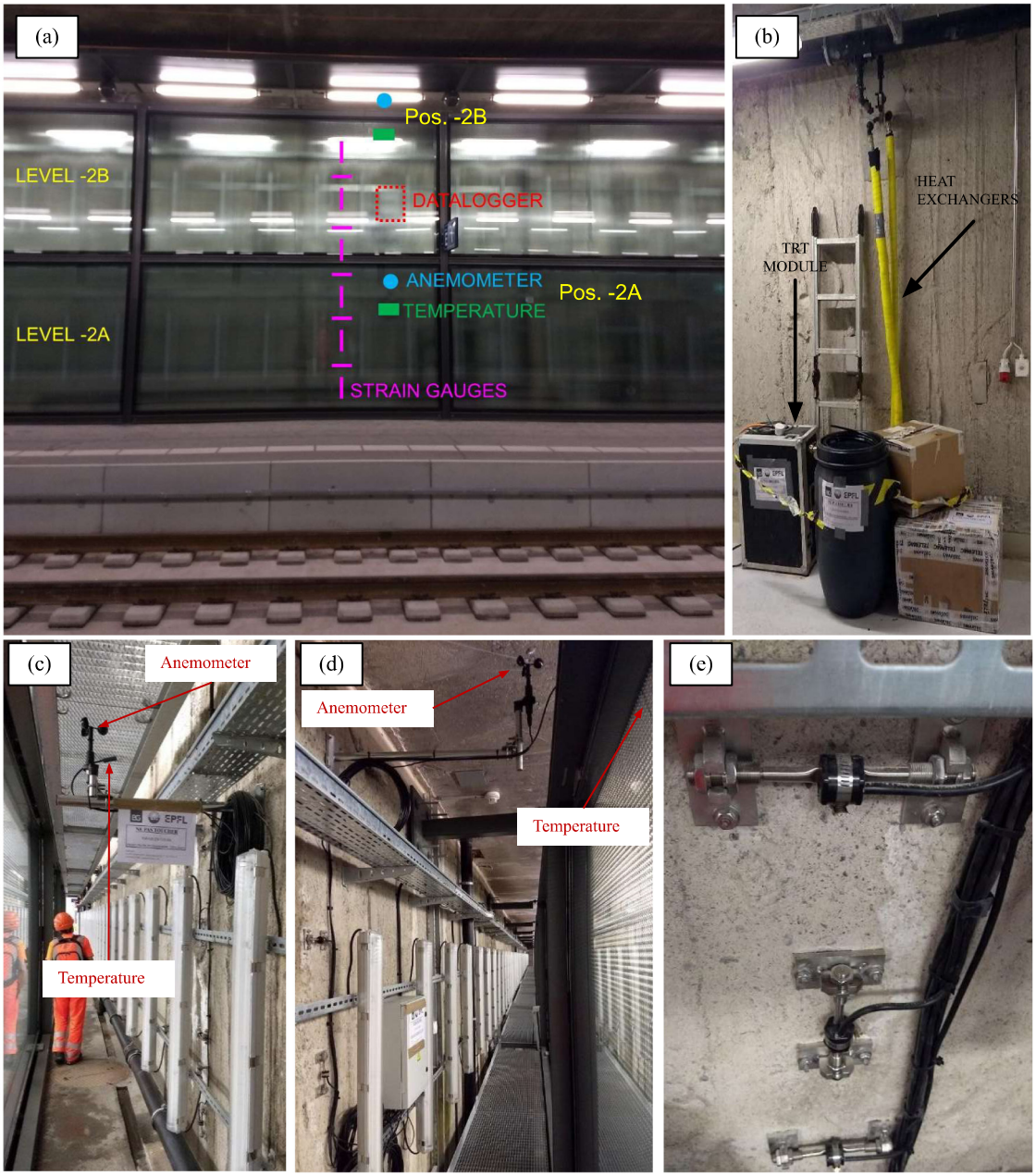

Fig. 2. (a) Global view of level -2 with an indication of the monitoring system; (b) details of level -1 with a description of the equipment used to perform the geothermal tests; (c) temperature sensor and anemometer at level -2 A; (d) temperature sensor and anemometer at level -2B; and (e) partial view of the strain gauges.

A technical room is located at level -1. The train station entrance for the passengers is at the ground level (level 0).

The vertical walls surrounding the train station and the base slab are equipped with HEs. The vertical walls are equipped with one U-loop every 2.5 m in the tunnel longitudinal direction, with a pipe spacing of 0.25 m and external and inner pipe diameters of 25 mm and 23 mm, respectively. The total length of each heat exchanger circuit in the walls is 36 m. The HEs are installed inside the concrete geostructure, attached to the reinforcement cage and placed at a distance 0.20 m from the wall-soil interface. The walls are 1 m thick, which means that the HEs are placed at a distance 0.80 m from the wall–air interface facing the tunnel. The 2.2 m thick slab is equipped with heat exchanger loops having a slinky shape and pipe spacing of 0.5 m. Every heat exchanger circuit in the wall and slab is connected in parallel to the main pipe connections. The entire piping system is eventually collected in a technical room. The portion tested in this study is composed of one single heat exchanger U-loop of the wall. The authors were not allowed to test larger portions of the UEI because of access restrictions.

The soil profile (Fig. 1) is characterized by a backfilling layer in the first 2.0 m, a layer of normally consolidated (NC) clay until a depth $z = -17.6$ m, a layer of slightly overconsolidated clay (OC) until $z = -23.6$ m, and a layer of dense gravel at the bottom, which hosts the groundwater table. During soil characterization, all soil layers were fully saturated, as from the analyses on samples taken from the site. Table 1 reports the material properties, where E is the Young modulus, ν is the Poisson ratio, γ_{sat} is the unit weight for saturated conditions, n is the porosity, and α is the thermal expansion coefficient. The material properties for the NC clay and OC clay are determined on the basis of an analysis of samples taken from the site. The material properties of the

Table 1
Material properties.

Material	Thickness (m)	E (MPa)	ν (–)	γ_{sat} (kN/m^3)	n (–)	α_{th} (K^{-1})
Backfill	1.92	30	0.30	19.6	0.35	10^{-5}
NC clay	15.60	19.9	0.30	19.7	0.35	10^{-5}
OC clay	5.98	41.6	0.30	20.2	0.37	10^{-5}
Gravel	37.91	150	0.25	22.5	0.21	10^{-5}
Reinforced Concrete	Structural geometry	28000	0.25	26.7	0.10	10^{-5}

backfilling and gravel materials were determined on the basis of a literature review.[13,14] Thermal properties are estimated through a dedicated in situ test (i.e., the TRT), as described in the following Section 4.2.

2.2. The testing campaign

The testing campaign contained two phases. First, a TRT was executed in August 2019, following the available standards.[15] Second, heat pump (HP) tests were performed, which allowed us to execute heating and cooling tests at constant inflow temperature and simulate real geothermal operation scenarios. HP tests were executed in December 2019 (heating) and March 2020 (cooling). To execute and monitor the experimental tests under different geothermal operation modes, a dedicated monitoring system was designed by the authors to monitor the hydrothermal behavior of the heat carrier fluid (HCF) inside the heat exchangers and the hydrothermal behavior of the air environment at levels -1 and -2 and to record wall intrados deformations at level -2 (Fig. 1 and Fig. 2). The experimental equipment used during the tests is installed at two levels (-1 and -2), which are separated and do not communicate with one another.

The equipment installed at level -1 is, in the first stage, the heating module, called the TRT module,[16] which is connected to the HE circuit Fig. 2(b). The TRT module applies constant thermal power to the HE circuit, as is usually employed for standard TRTs.[16–20] In a later stage, the TRT module was replaced by a water-to-air HP (i.e., a commercial heat pump: Ciat Ereba 11HT He), which allows heating/cooling tests to be performed by imposing the temperature at the inflow point of the HE circuit (i.e., the HP outflow). For the TRT module and the HP, a dedicated hydrothermal monitoring system is installed, allowing continuous (i.e., one record every 30 s) monitoring of the following parameters: (*i*) the HCF temperature at the inflow and return end of the HE circuit, (*ii*) the HCF flow rate, and (*iii*) the air temperature at the HP ventilator, inside the TRT module and of the undisturbed air of level -1.

The equipment installed at level -2 consists of a thermomechanical monitoring system (Fig. 2(a)) specifically designed for this tested site.[21] The monitoring system is designed to allow the measurement of key parameters that govern the heat fluxes and the hydrothermal heat exchanges between the EG and tunnel air, as well as the wall intrados deformations. It allows real-time monitoring (i.e., one record every 5 min) of (*i*) air temperature and (*ii*) the wind speed in the tunnel and (iii) structural deformations at the wall intrados. Air temperature and velocity are measured through temperature sensors and anemometers (i.e., a resolution of 0.1 °C for temperature and 0.05 m/s for wind velocity) placed at two locations (pos. -2 A and pos. -2B in Fig. 2(a, c, d)): at the top part in front of the glass wall (i.e., Pos. -2B) to monitor the train station environment; in the bottom part behind the glass wall (i.e., Pos. -2 A) to monitor the environment behind the glass wall. Structural monitoring is performed by employing deformation sensors (i.e., 11 uniaxial, vibrating wire strain gauges that read strain and temperature with a resolution of 1$\mu\epsilon$ and 0.1 °C, respectively) that are screwed to the wall intrados and installed, alternatively, in the vertical and longitudinal directions (Fig. 2(e)). The air temperature distribution near the wall intrados is captured through strain gauge readings. All the instruments are connected to a datalogger installed at level -2B. Because the geostructure was already partly constructed at the time of these experiments and the ground surface was a construction site, there was no possibility to install any monitoring system in the soil or inside the concrete geostructure. The data collected through this monitoring system enable a detailed assessment of the hydrothermal behavior of the train station environment (i.e., a time series of air temperature and wind speed) from August 2019 until June 2020. These experimental data allow for a detailed assessment of the boundary conditions of the numerical model reported in this work.

The experimental tests involving thermal activation of the HE circuit were of different types. First, a TRT was executed in August 2019. This test contained two phases: An initial phase of fluid circulation lasted 2 days, followed by the heating phase at a constant thermal power $Q_{th} = 1$ kW $= 45$ W/m of wall depth for 24 days. Second, the heat pump tests involved HCF heating (i.e., imposed inflow temperature $T_{f,in} = 50.0$ °C) and cooling (i.e., $T_{f,in} = 1.0$ °C) tests and were performed between December 2019 and March 2020. Each test lasted approximately 2 weeks.

3. Hydrothermal behavior: experimental results

This section presents the results related to (*i*) the hydrothermal behavior of the train station and the experimental results of the (*ii*) TRT and (*iii*) heating/cooling HP tests.

3.1. Hydrothermal behavior at the train station level

The train station hydrothermal behavior is detailed here with reference to (*i*) its seasonal temperature evolution with correlation to the ground surface environmental temperature and (*ii*) the wind speed profile and the interactions with the train circulation effects. The monitored results are compared with the surface temperature measurements taken by Météo Suisse at the Genève Airport weather station.

From the thermal interactions between the tunnel and ground surface (i.e., external) temperature evolution, two behaviors are apparent (Fig. 3). From August to October and from March to June, the tunnel temperature follows periodic behavior daily, which is lower than the external temperature during the day and higher at night. During a period, the average difference between the tunnel and external temperatures is, in absolute terms, approximately 6.0 °C and 4.0 °C for day and night, respectively. The tunnel temperature varies between 12.2 °C and 30.1 °C. The external temperature varies between −2.5 °C and 33.8 °C. The temperature recorded at position -2B is generally higher than that at position -2 A. From the end of October to March, the tunnel temperature behaves periodically on a daily basis and is always (i.e., during day and night) higher than that recorded outside. The difference between the tunnel temperature and external temperature varies between $3 \div 5$ °C. The tunnel temperature varies between 6.5 °C and 13.0 °C. The external temperature varies between −5.5 °C and 13.1 °C. The minimum values are lower at position -2B than at -2 A.

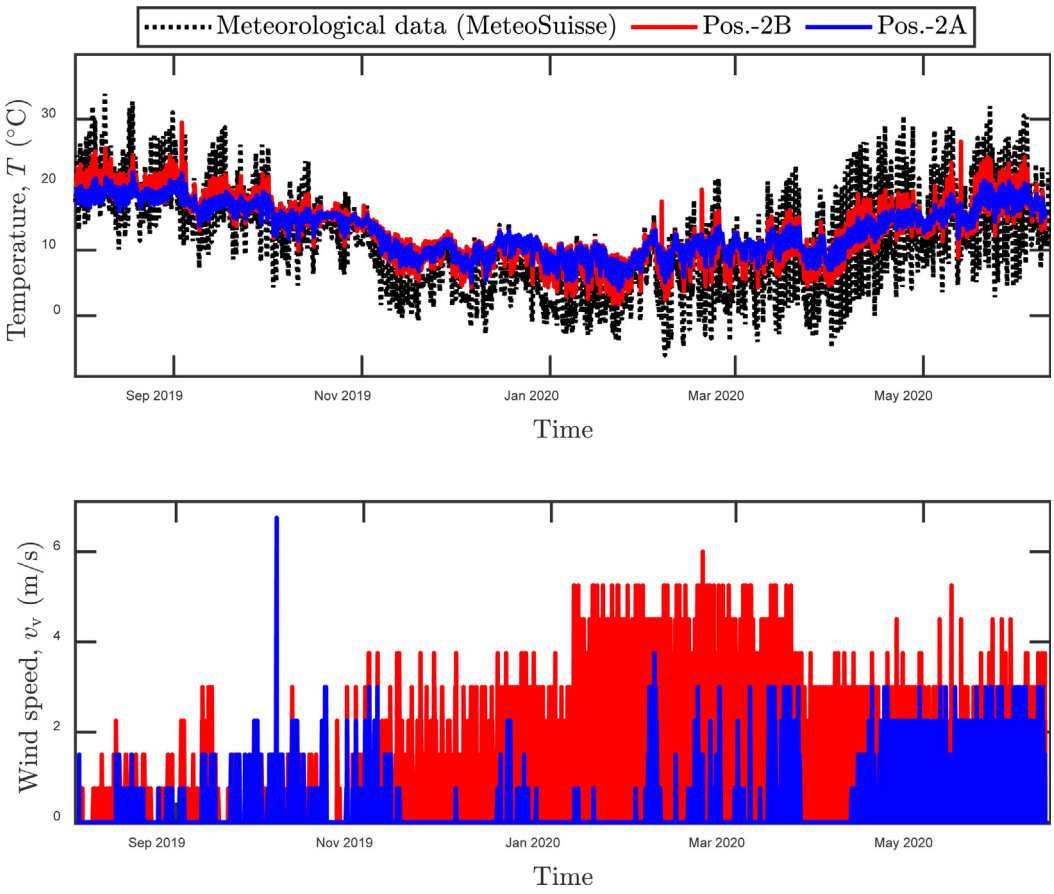

Fig. 3. Tunnel air temperature evolution and wind speed from the end of July 2019 to the beginning of June 2020.

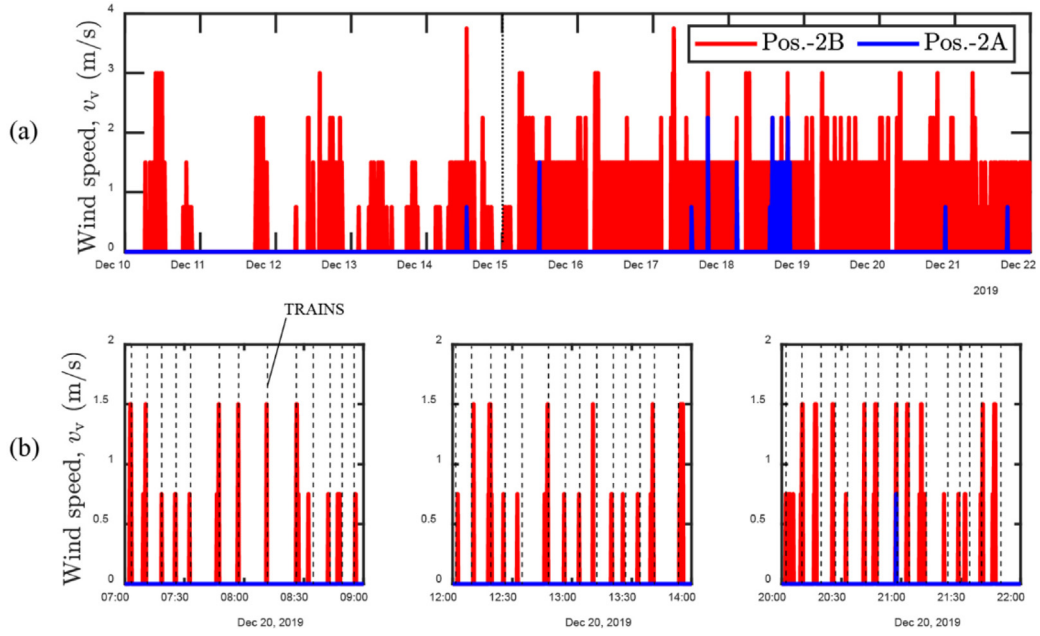

Fig. 4. Measurement of wind velocity: (a) global view of the behavior before and after the beginning of train circulation (i.e., on Dec. 15); (b) magnified view at three times during a typical day after train traffic circulation starts and correlations between the wind speed measurements and train passages.

The wind speed profile (Fig. 3) shows two behaviors, occurring before and after the start of train traffic circulation (i.e., on December 15th, 2019, Fig. 4(a)). Before the start of train traffic circulation, wind speed values greater than 0.5 m/s (i.e., the lower operational limit of the instrument) are recorded sporadically. A limited difference between the values measured at positions -2 A and -2B is reported. After the start of train traffic circulation (Fig. 3 and Fig. 4), more frequent wind speeds higher than the thresholds are recorded. This behavior is described in detail in Fig. 4, which reports the overall airflow behavior before and after

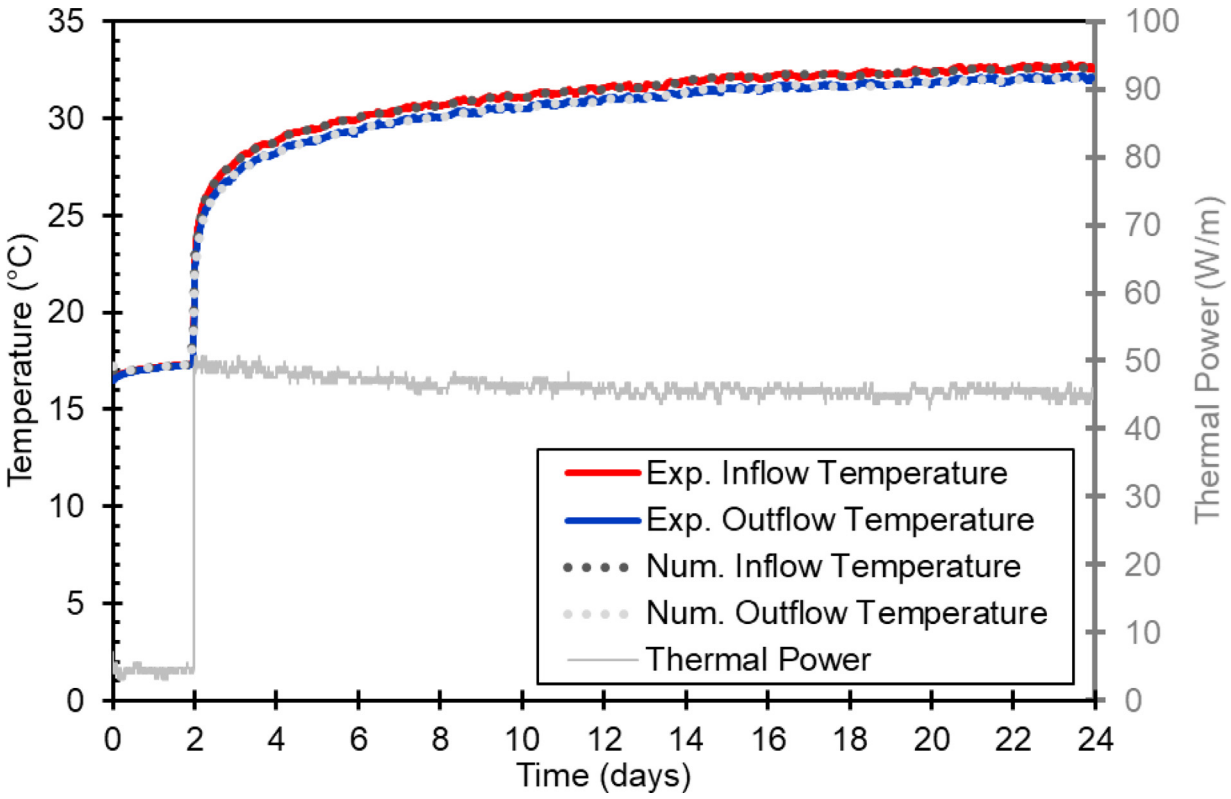

Fig. 5. Experimental data from the TRT module (fluid temperature and thermal power) with fitting of the numerical results.

Table 2
Determination of the yearly temperature profiles for each boundary condition.

	External temperature (ground surface) T_{gs} (°C)	Tunnel temperature T_t (°C)	Technical room temperature T_{tr} (°C)
Jan	2.2	6.0	11.0
Feb	2.9	8.0	10.0
Mar	6.9	11.0	12.0
Apr	11.0	15.0	13.5
May	14.7	18.5	17.0
Jun	19.2	21.0	19.0
Jul	20.8	22.0	21.0
Aug	20.0	21.0	21.0
Sep	16.0	18.5	18.5
Oct	11.7	15.0	16.0
Nov	6.4	11.0	13.5
Dec	2.9	8.0	11.5

the beginning of train circulation (Fig. 4(a)), denoting periodic daily behavior after December 15, 2019. Fig. 4(b) shows the correlation between air speed measurements and the passage of trains at three times of a typical day (i.e., morning, afternoon, evening). The peaks of the air speed values coincide perfectly with the train passages, which were taken by studying the train timetable available at the train station.

3.1.1. Definition of the yearly temperature profiles near the underground energy infrastructure

The measurements allow us to reconstruct the yearly temperature profiles in the environments located near the UEI that affect thermal exploitation. These values, which are summarized in Table 2, are also used as boundary conditions for the numerical model that simulates the in situ tests, as presented in Section 4.

3.2. TRT

The test started with a fluid circulation phase (i.e., no heating), which lasted 2 days. The duration was chosen after running a preliminary test a few weeks in advance, with a duration of one week, that showed no fluid temperature fluctuations on a day/night basis. The heat injection phase at constant power lasted 24 days, which is considered sufficient to reach the steady state.

During the fluid circulation phase, the fluid temperature reached a constant value of $T_{f,exp} = 17.3$ °C, which represents the average temperature of the wall subjected to the effects linked to the soil, tunnel and ground surface temperatures (Fig. 5). This value is slightly higher than the average soil temperature values recorded for European climates,[16,22,23] suggesting that the soil temperature distribution could be affected by the presence of the tunnel. During the heating phase (i.e., application of constant power), the fluid temperature rapidly increased. Two distinct periods are clearly distinguished: an initial, transient phase of approximately $5 \div 7$ days is followed by a steady state condition, in which the fluid temperature slowly increases with time (Fig. 5. The temperature difference between the inflow and outflow remains constant throughout the heating phase and is equal to $\Delta T_f = 0.6$ °C.

3.3. Heat pump tests

To test the UEI behavior under realistic heating/cooling operation modes, additional tests were executed. The equipment used during these tests consists of a water-to-air heat pump (HP) located at level -1, which replaces the TRT module. A dedicated hydrothermal monitoring system is designed for this installation. This monitoring system allows for continuous measurement of (*i*) inflow and outflow fluid temperatures, $T_{f,in}$ and $T_{f,out}$, respectively; (*ii*) the flow rate, $\dot{V}$, of the HCF; (*iii*) the air temperature at the HP ventilator, $T_{ventilator}$; and (*iv*) the technical room temperature, T_{tr}. Heating and cooling tests at constant inflow temperature were executed between December 2019 and March 2020 to simulate realistic summer and winter operations, respectively. The HP allows for setting a user-defined $T_{f,in}$, and it automatically sets the time-dependent behavior of the internal circulation pump (i.e., settings of flow rate) to ensure the best functioning and respect for the maximum and minimum internal temperatures to avoid any excessive heating and/or fluid freezing.

The objectives of these tests are to reach limiting values (maximum and minimum) of the HCF temperature representative of future UEI operations. In other words, these tests aim to represent worst-case scenarios in terms of the temperature difference imposed on the UEI from a thermomechanical viewpoint and best-case scenarios in terms of thermal exploitation (i.e., highest thermal power). In the following, the results for heating and cooling tests are reported and discussed.

3.3.1. Heating tests

A heating test was executed in December 2019. The time of year in which the tests were performed was imposed by the construction site's tight schedule. Heating tests represent the summer behavior of a UEI: heat is injected in the ground to produce fresh air used for air conditioning of the superstructure. The heating test performed in this context aims at achieving high temperature levels in the range of values normally used in low enthalpy geothermal applications and for heat storage operations.[24–28] During heating tests (i.e., summer operation), the HCF is therefore cooled by exchanging heat with the surrounding materials, which are at a lower temperature than that imposed by the heat pump. As a result, the wall and soil are heated. Finally, the heat pump, via its refrigerating internal cycle, produces fresh air.

Heat injection at constant temperature was performed by fixing $T_{f,in} = 50.0$ °C. The observed HP behavior is continuous and cyclic (Fig. 6(a)), with approximately 2 cycles per hour. The heat pump is switched on for approximately 15 min, when $T_{f,in}$ increases to the set value, and then for approximately 15 min, $T_{f,in}$ gently decreases to allow for thermal recharging around the HEs. $T_{f,in}$ varies between $45.0 \div 56.5$ °C. $T_{f,out}$ varies accordingly, with a slight time shifting of a few seconds. The average HCF temperature variation between the outflow and inflow is $\Delta T_f = T_{f,in} - T_{f,out} = 5.9$ °C. The flow rate varies between $\dot{V}_f = 18 \div 27$ L/min. The average thermal power injected (i.e., negative) by HP operation is $Q_{th,f} = -7$ kW. A global view of the heating test is provided in Fig. 7(a).

3.3.2. Cooling test

A cooling test was performed in March 2020. The cooling test represents the winter behavior of a UEI: a cold HCF is injected into the HEs, and by extracting heat from the surroundings, the fluid is heated until the outlet point. It follows that the materials within the UEI (i.e., pipes, wall, soil and tunnel) are cooled as heat is extracted by the HCF. During this operation, the HP produces hot air for heating the superstructure. The cooling test performed here aims at achieving the lowest values of HCF temperature allowable by the HP, simulating a real winter operation.[3,7,10–12,29–33]

The inflow temperature was set to $T_{f,in} = 1.0$ °C. The heat pump response was highly discontinuous on a periodic basis (Fig. 6(b)). The HP switched on for a limited period (i.e., approximately 25 min per hour) and then switched off, stopping the imposition of the inflow temperature but allowing the fluid to circulate at ambient temperature. In this way, temporary thermal recharge of the materials surrounding the HCF was possible, and heat extraction could afterwards resume. This strongly intermittent, periodic behavior occurred because the minimum allowable HCF temperature value was reached, and the HP needed to stop to avoid freezing issues. The inflow temperature ranged between $T_{f,in} = 0.5 \div 9.2$ °C. The outlet temperature varied between $T_{f,out} = 2.3 \div 8.2$ °C. The average inflow-outlet fluid temperature difference was $\Delta T_f = 2.5$ °C. The flow rate ranged between $\dot{V}_f = 12 \div 24$ L/min. The average thermal power extracted (i.e., positive) was $Q_{th,f} = 2$ kW. A global view of the cooling test is shown in Fig. 7(b).

4. Hydrothermal behavior: numerical modeling

4.1. Features of the numerical analyses

A 3D finite element model (i.e., thermomechanical, featuring for the non-isothermal fluid flow in the HE) used to simulate the in situ test and to interpret the results is built using the software COMSOL Multiphysics.[34]

The objectives for the numerical analyses are (*i*) to help determine the thermal characteristics of the materials involved in the heat exchanges; (*ii*) to give a comprehensive overview of the hydrothermal behavior of the UEI, highlighting the soil temperature distribution before and during the tests, the volume of materials affected by the thermal exchanges, and the direction and magnitude of the wall–tunnel and wall–soil heat fluxes; and (*iii*) to study the thermomechanical behavior. Some of the parameters measured experimentally are input parameters for the numerical model (e.g., inflow temperature and velocity, boundary conditions), while others are back-analyzed to calibrate the numerical model to best fit the experimental data (e.g., thermal characteristics of materials). The model dimensions are 186 m × 55 m × 100 m in the *x*-, *y*-, and *z*-coordinates (Fig. 8). The HEs are modeled following the technical details of the geostructural design. The soil and structure are modeled as fully saturated porous materials. The groundwater is considered in stationary condition with null velocity; hence, convective heat exchanges within the soil are neglected. The mathematical formulation and details of the numerical model are reported in Appendix A.

The thermal boundary conditions (Fig. 8) are as follows: the two vertical surfaces at the sides are adiabatic (i.e., the far-field temperature distribution with depth is not affected by the tunnel, and the surface temperature affects the top 15 m, simulating realistic far-field conditions); the front and rear vertical surfaces are adiabatic; the bottom horizontal surface is set to a constant temperature, T_s (i.e., the soil temperature); and the ground surface, technical room and tunnel air interfaces are simulated by means of convective boundary conditions (i.e., flux conditions, $\dot{q}_i$), setting a coefficient for convective heat transfer, h_i, and an air temperature, T_i, based on experimental results. h_i is linked to the air velocity and is calibrated following the available correlations.[35–39] h_i was chosen as $h_{gs} = 10$ W/m^2/K, $h_{tr} = 3$ W/m^2/K, and $h_t = 4$ W/m^2/K for the ground surface, technical room and tunnel, respectively; the first coefficient represented a wind velocity of approximately 1 m/s, and the latter coefficients represented a "quasi-zero" wind velocity. T_i are transient functions set as in Table 2. The mechanical boundaries are as

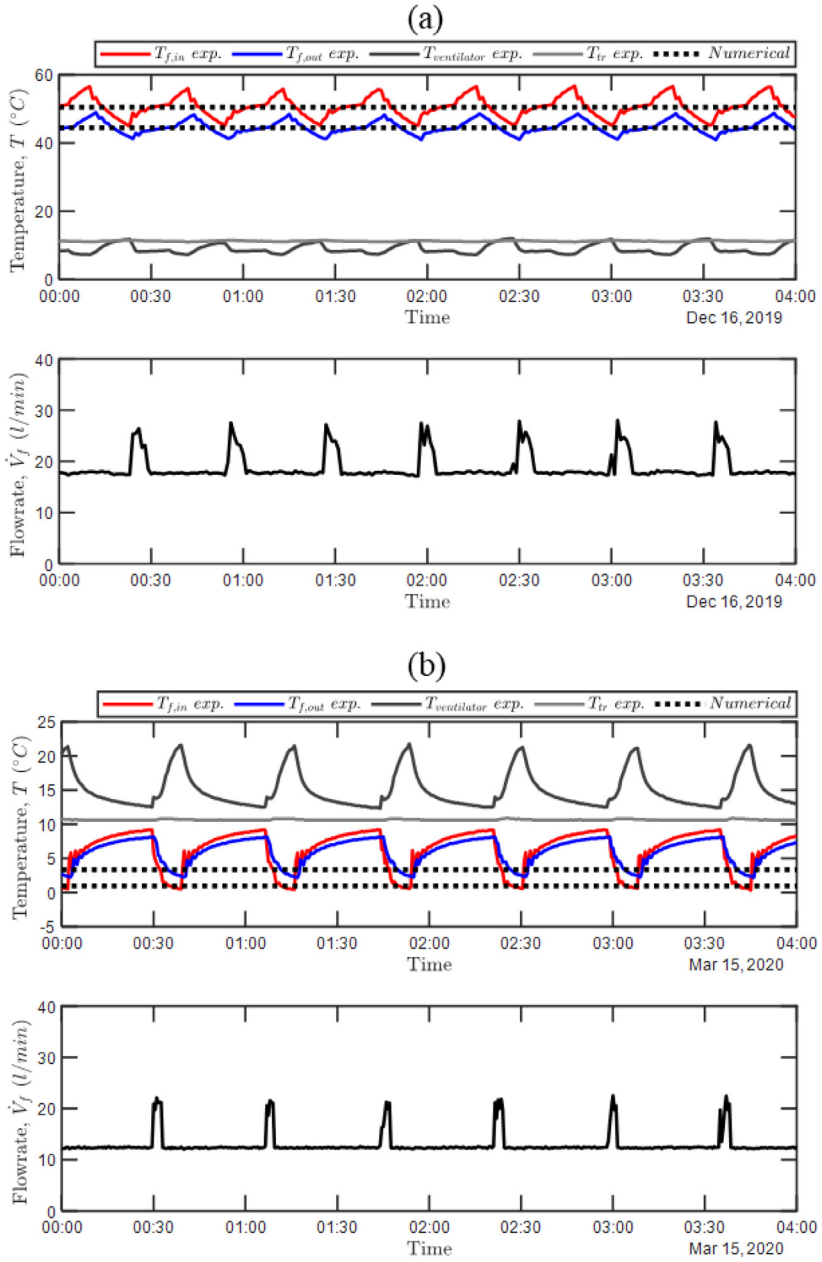

Fig. 6. Magnified view of HP behavior during different cycle types: (a) heating test, December 2019 and (b) cooling test, March 2020.

follows: the base boundary is fixed, and all the vertical boundaries are rollers, while the remaining boundaries are free (Fig. 8). The nonisothermal fluid flow in the HE is simulated by imposing the experimental time history of fluid inflow temperature and velocity, while the outflow fluid temperature is used to calibrate the model with respect to the experimental results. The solver accounts for a temperature initialization phase of 10 years duration to ensure that the result is independent of the model initial condition, followed by simulating the experimental tests. During such period, the periodic thermal boundary conditions (Table 2) are applied so that to obtain a realistic temperature initialization before the start of geothermal operations. Further outcomes on this aspect are reported in Section 4.3.

4.2. TRT

The objectives of numerical modeling are to interpret the experimental results, giving a full picture of the hydrothermal aspects involved in UEI operation. The TRT is usually employed in geothermal applications[10,12,20,35,36,40,41] to thermally characterize the materials surrounding a thermoactive element (e.g., borehole, pile), determining (*i*) the undisturbed soil temperature and (*ii*) the average thermal conductivity of the soil. Numerical techniques are adopted instead of, for example, analytical and/or semianalytical techniques for addressing these challenges because of the geometrical complexities and the highly transient thermal behavior of the UEI and its boundary conditions (Fig. 3, Table 2).

The undisturbed soil temperature, T_s, is varied to obtain an average temperature in the HEs equal to that measured by the TRT module during the water circulation phase. This correspondence occurs for $T_s = 14.6$ °C, which is consistent with the expected values for the European climate. Before the start of the heating phase of the TRT, the average fluid temperature is $T_{f,num} = 17.30$ °C, which is very close to the experimental value, $T_{f,exp} = 17.34$ (Fig. 5).

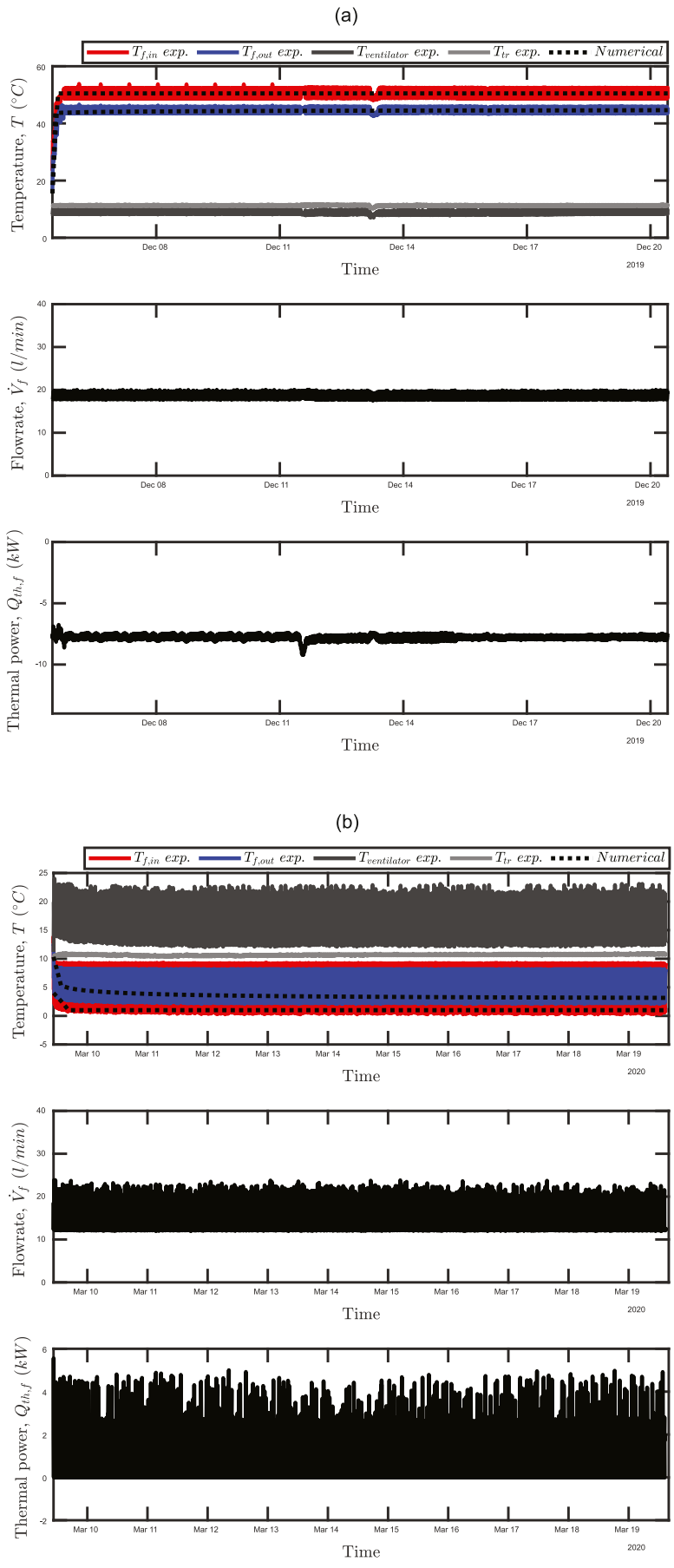

Fig. 7. Global view of the HP behavior during the experiments: (a) heating test (December 2019) and (b) cooling test (March 2020).

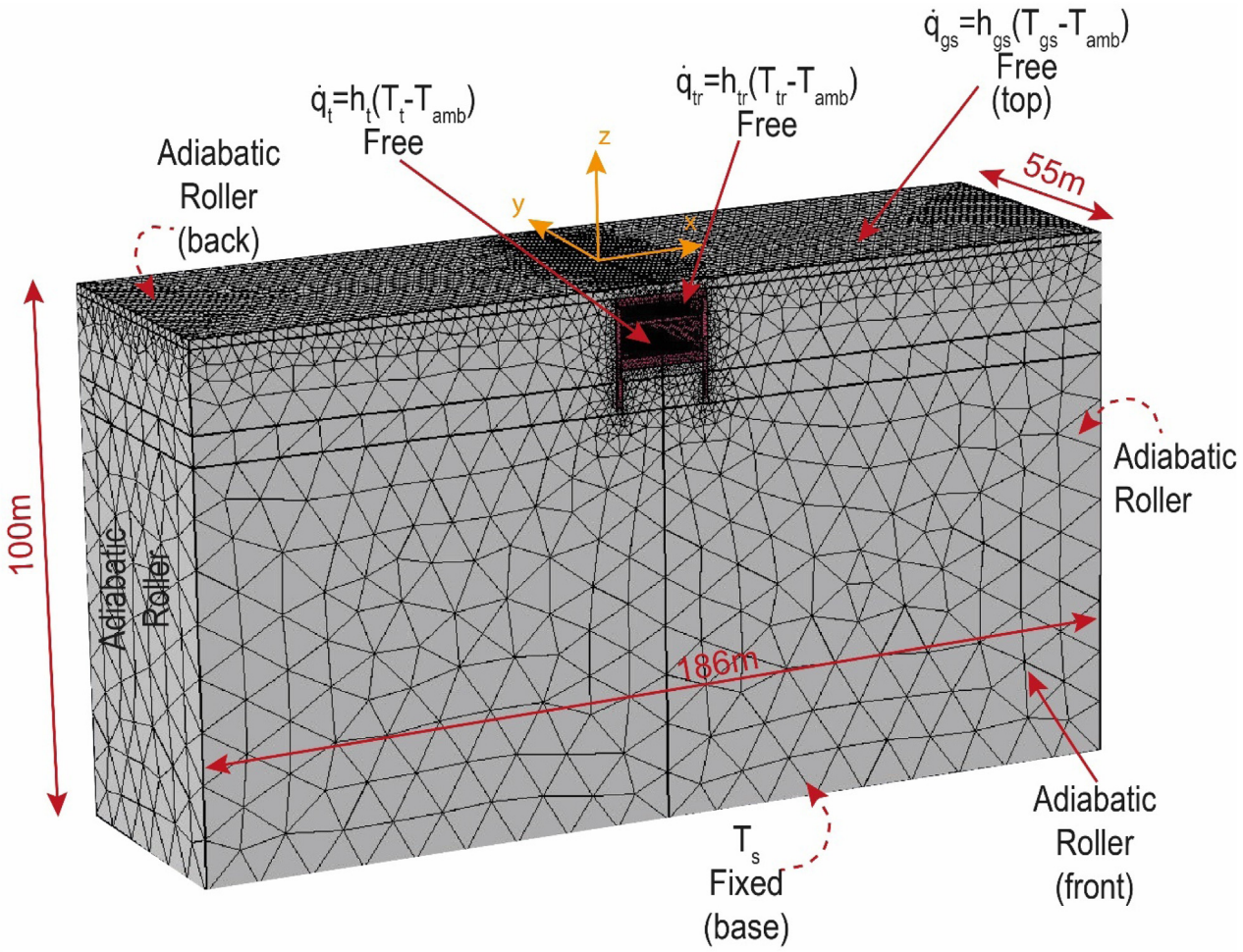

Fig. 8. Geometry of the numerical model with indication of the boundary conditions.

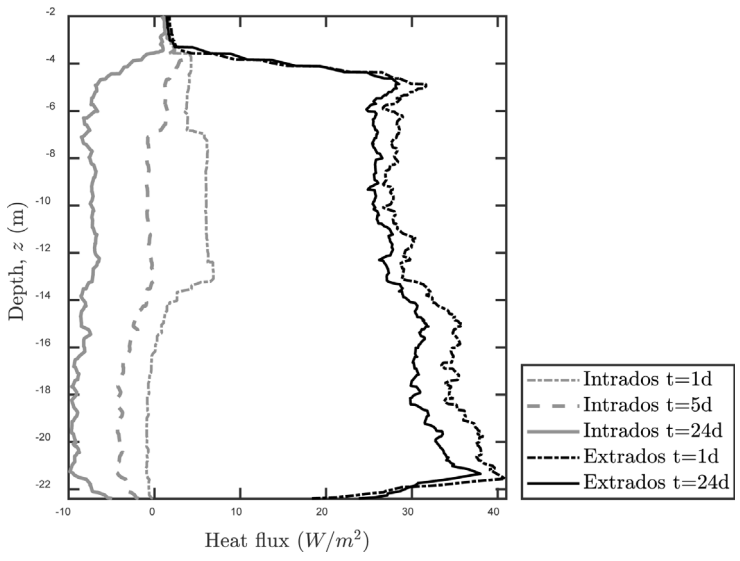

Fig. 9. Magnitude of heat flux at the wall intrados and extrados.

The estimate of the thermal characteristics of the involved materials (i.e., soil and concrete) represents the second objective. To do so, an issue related to the unicity of the solution exists: it is impossible to uniquely determine the thermal conductivity of soil and concrete while having only one experimental result. Concrete thermal conductivity could realistically vary between $\lambda_c = 1.0 \div 2.0$ W/m/K.[35,36,42–44] Soil thermal conductivity (i.e., normally consolidated clay and slightly overconsolidated clay in saturated conditions) could realistically be evaluated as $\lambda_s = 1.0 \div 2.5$ W/m/K.[1,45]

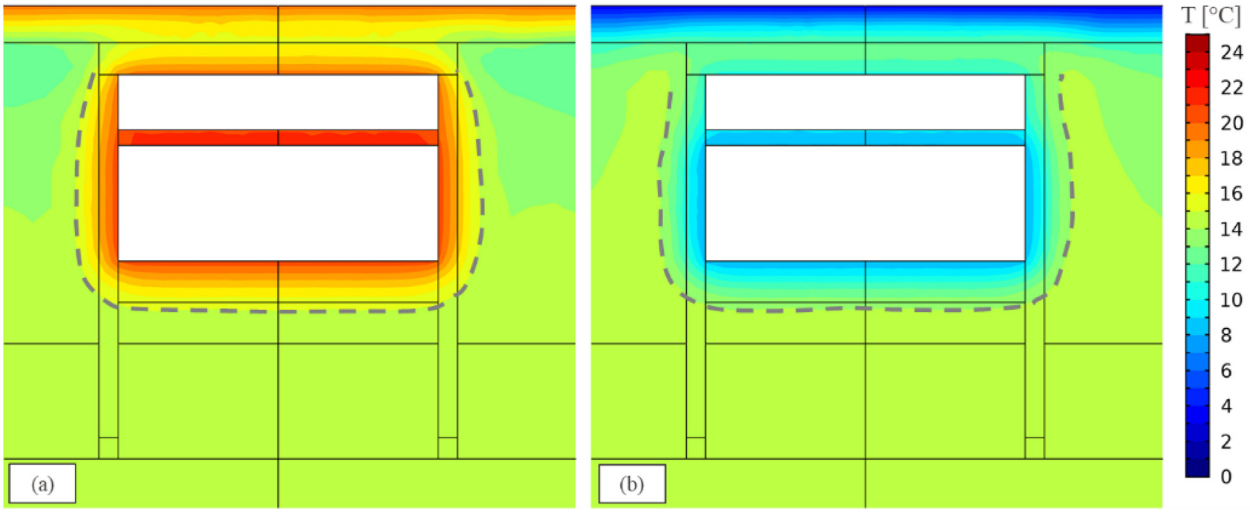

Fig. 10. Temperature profile (numerical results) within and around the UEI determined by applying the tunnel, technical room and surface boundary conditions: (a) summer and (b) winter. The dotted gray line denotes the portion of materials that undergoes the most severe temperature variations induced by applying boundary conditions.

Dedicated parametric studies are run to detect the impact of thermal capacity of soil and concrete in reproducing the experimental results. Thermal capacity plays a role during the transient phase of the TRT heating, which lasts approximately 2 days (Fig. 5). Then, the process is driven by thermal conductivity as a steady-flux condition is reached. Such analyses highlighted that very marginal effects are played by thermal capacity of concrete and soil. For such reasons, thermal capacity and density are fixed to $Cp_c = 850$ J/kg/K, $\rho_c = 2722$ kg/m^3, $Cp_s = 1000$ J/kg/K, and $\rho_s = 2011$ kg/m^3 for concrete and soil, respectively.[1,35,36,41,45] A sensitivity analysis of thermal capacity effects was performed, showing little variation in the UEI thermal performance. Concrete thermal conductivity was fixed to different values, and soil thermal conductivity was evaluated to best match the experimental results (Table 3). The comparison between the experimental and numerical results was performed at the outflow fluid temperature, $T_{f,out}$, which is not an input parameter of the numerical model. The error is evaluated as $T_{f,out,num} - T_{f,out,exp}$, as reported in Table 3. In the following, the numerical results for $\lambda_c = 1.7$ W/m/K and $\lambda_s = 1.4$ W/m/K are reported, as they represent the best fitting to the experimental results. Close agreement between the experimental and numerical results is reported in Fig. 5.

Additionally, numerical analyses give a broader view of the thermal response of the UEI during TRT execution, with emphasis on (*i*) the temperature profile of the materials upon heating, (*ii*) heat fluxes and (*iv*) intrados tunnel temperature.

At the beginning of the heating phase, the soil is strongly affected by thermal exchanges because of the vicinity of the HE: consequently, the heat exchanger-soil heat flux (i.e., extrados) slightly decreases with time due to heat propagation in the soil and the increase in the soil volume affected by temperature variations. The extrados heat flux range is between $25 \div 35$ W/m^2 (Fig. 9). At the end of the test, the model suggests that a soil portion of thickness 1.5 m around the EW is affected by a temperature variation of > 1 °C with respect to its initial temperature distribution.

The temperature distribution inside the concrete geostructure evolves with time. At the beginning of heating and during a portion of the transient condition, the intrados temperature is higher than that of the HCF. It follows that the heat flux is directed from the tunnel toward the HCF. The tunnel, in this phase, acts as a thermal resistance rather than as a conductor (Fig. 9), where a positive heat flux denotes a flux vector directed toward the positive *x*-axis (i.e., from the wall toward the soil). The tunnel is located between $z = -7.5$ m and $z = -14$ m, and a positive heat flux with a magnitude of approximately $+7.5$ W/m^2 is recorded. When the HCF temperature increases, it becomes higher than that of the tunnel, hence reversing the heat flux. It reaches its stationary condition at approximately -10 W/m^2. The heat fluxes are hence dominated by the extrados component, which is $3 \div 5$ times higher than the intrados component.

Thermal photos at level -2 were taken on the last day of testing and compared with the numerical results, showing close agreement (complementary results are available in Ref. 21). The longitudinal thickness of the intrados thermally affected zone is 2.5 m. The intrados temperature varied between $20 \div 22$ °C on 21/08/2019 and between $20 \div 23$ °C on 29/08/2019. It follows that the temperature distribution inside the wall is nonuniform: it shows a maximum located near the HCF. The temperature decreases until reaching a minimum at the wall–tunnel interface.

4.3. Heat pump tests

The heat pump tests are numerically simulated using the same model presented above. Inflow temperature is imposed as the average monitored $T_{f,in}$, while the outflow temperature is used for comparison among the numerical and experimental results. To reduce the computational cost, the numerical model cannot capture each HP cycle, but the average inflow and outflow temperatures are in close agreement with the experimental results for the heating (Fig. 6(a)) and cooling (Fig. 6(b)) tests.

Before analyzing the details of the wall–tunnel interactions during the thermal activation tests, it is worth analyzing the UEI-tunnel interactions induced by the application of boundary conditions only. As reported in Table 2, the temperature profiles at the boundaries present yearly periodic behaviors. These conditions have implications on the UEI operation, as they modify the temperature profile of the UEI itself and its surroundings. A portion of the wall and soil undergoes a seasonal temperature variation of $\Delta T \cong 6 \div 10$ °C (Fig. 10). The concrete presents maximum/minimum temperatures of $T_c = 19 \div 9$ °C during summer and winter. The soil (i.e., the portion within the dashed gray lines reported in Fig. 10) presents $T_s = 17 \div 11$ °C during summer and winter. These temperature variations must be considered

Table 3
Evaluation of thermal conductivity for concrete and soil: determination of soil thermal conductivity to best match the experimental results for a given concrete thermal conductivity.

Concrete thermal conductivity $\lambda_c \left(\frac{W}{mK}\right)$	Soil thermal conductivity $\lambda_s \left(\frac{W}{mK}\right)$	Absolute numerical-experimental error at steady state (°C)
1.7	1.4	0.014
1.5	1.9	0.026
1.2	2.1	0.044
1.0	2.4	0.045

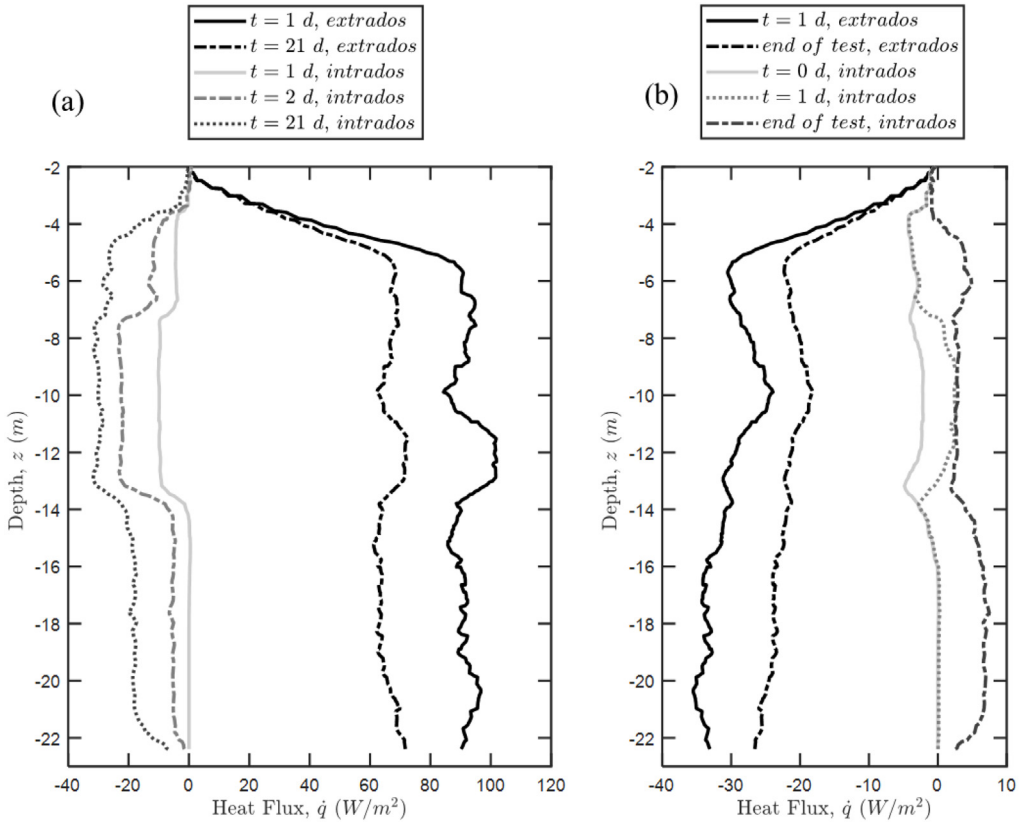

Fig. 11. Intrados and extrados heat fluxes: (a) heating test and (b) cooling test.

when studying UEI operation for two reasons. First, temperature variations induced by natural effects on the order of magnitude of several degrees Celsius may affect the validity of the hypothesis of "yearly constant soil temperature", which is often applied to energy geostructures.[1] Second, Fig. 10 shows that the portion of materials that undergoes these temperature variations represents more than 50% of the volume of the most thermally affected materials during UEI operation. It follows that these environmental temperature variations will affect the UEI operation, as the tunnel heats the materials during summer and cools them during winter, reducing the seasonal potential for heat injection and extraction, respectively. This reduction is already partly apparent in the HP results for the cooling test (Section 3.3.2), as the heat pump must periodically stop to allow for thermal recharge before resuming its operation. This effect is detrimental to winter operation: a reduction in the average temperature of materials reduces the potential for cooling the UEI, as the allowable operative temperature range is already limited from most operative prescriptions and available standards.[15,46,47]

Analyses of the hydrothermal behavior during heating and cooling tests are reported here. Upon heating, the maximum portion of materials affected by thermal effects extends up to 2 m of soil laterally to the UEI. The maximum wall temperature is $T_{w,max} = 38.0$ °C. The magnitude of the intrados heat fluxes is transient. The wall and tunnel act as conductors, with the heat flux magnitude increasing as the heating persists. The extrados heat flux strongly dominates the intrados heat flux (Fig. 11(a)). The heat flux at the extrados is slightly higher for the top portion of the wall (i.e., facing the tunnel level) than for the bottom portion because the initial soil temperature is lower. The magnitude of the heat flux at the extrados is thrice that at the intrados.

Upon cooling, the portion of materials affected by thermal effects extends up to 1 ÷ 1.5 m of soil laterally to the UEI, with the portion of soil affected by thermal effects increasing in volume as the cooling persists. The minimum wall temperature is $T_{w,min} = 4.3$ °C. The heat flux at the extrados is higher in the fully embedded portion of the wall that at the top part, contributing to the higher temperature difference between the soil and the HCF (Fig. 11(b)). The magnitude of the heat flux at the extrados is fivefold higher than that at the intrados.

The wall intrados is affected by temperature variations induced by the thermal activation of the UEI. Comparisons between experimental (i.e., thermal photos) and numerical results showed close agreement (complementary results are available in Ref. 21). Upon heating, the longitudinal extent of the intrados' thermally affected region was 2.5 m. The average temperature difference between the thermally affected and undisturbed portions was 3.5 °C. Upon cooling, the longitudinal extent of the

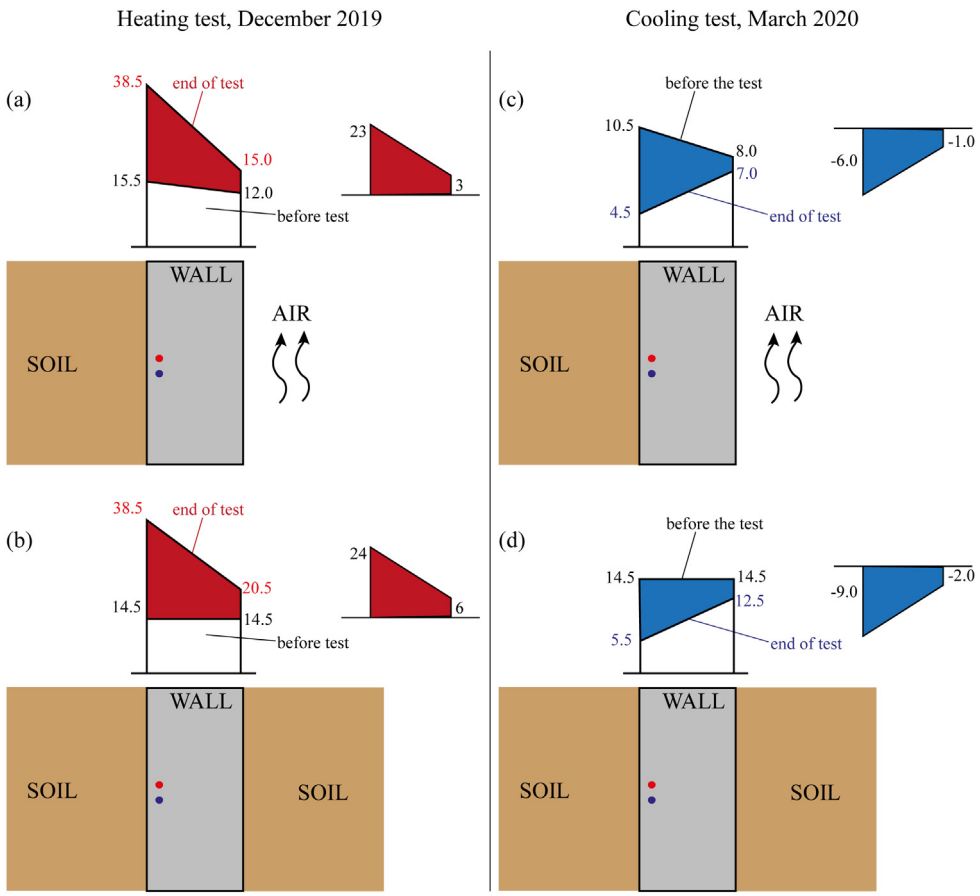

Fig. 12. Sketches of the temperature distributions in the wall: (a) upon heating, at the top part, facing the tunnel; (b) upon heating, at the fully embedded portion; (c) upon cooling, at the top part, facing the tunnel; and (d) upon cooling, at the fully embedded portion. The presented values are retrieved from experimental (where applicable) and numerical results. NOTE: the sketches are not scaled.

thermally affected portion was 1 m. The average temperature difference between the thermally affected and undisturbed regions was −1.5 °C. Close agreement between the experimental and numerical results was found.[21]

4.4. Preliminary guidelines for TRT execution and data interpretation for underground thermoactive infrastructures

This section discusses the details of the execution of TRTs applied to UEIs and, more generally, to any geostructure partly in contact with an air interface. To our knowledge, no literature on this topic is available. Moreover, no feedback, execution manuals or legislative standards for test execution or data interpretation are available.

TRT-type heating input was extensively used to determine the soil thermal characteristics for vertical HEs[16,18] and energy piles and to detect the thermomechanical behavior of energy geostructures.[6,23,48–50] Consequently, the first challenge was to understand what knowledge the execution of TRT on UEIs could bring, knowing that the focus should be on determining the thermal behavior and potential of the UEI. On the basis of the foregoing presented results, the main feedbacks are reported here.

First, one should verify that the following criteria are fulfilled when performing the test: (*i*) the fluid circulation phase should last long enough so that possible day/night fluid temperature variations are recorded; (*ii*) the heating phase should last long enough so that the steady state condition within the HE is successfully reached. In this regard, the typical heating duration used for vertical HEs (i.e., one week) should be taken as a lower boundary. The longer and/or the more complex the heat exchanger circuit is, the longer the heating phase should be to ensure that it reaches the steady state. Additionally, the stronger the hydrothermal interactions with neighboring environments (e.g., air interfaces) are, the longer the time needed to reach steady state conditions is. (*iii*) The interpretation of the results requires a detailed, time-dependent knowledge of the thermal environment characterization near the UEI. The definition of the initial temperature profile within and around the UEI is crucial. (*iv*) If the thermal environments around the UEI are not known with sufficient accuracy, the installation and use of a dedicated in situ monitoring system is strongly advised. (*v*) The interpretation of the results should account for all relevant heat exchange modes occurring within and around the UEI. Consequently, the use of numerical models seems to be the most accurate tool in view of the presence of geometric complexities. Attempts to determine the soil thermal conductivity using analytical models[16,51] were made in the case presented in this study. The multiple, concurrent, thermal processes lead to a complex definition of the heat fluxes direction, and make the assumptions of the simplified analytical models unsuitable for the analysis of the geometry in question (e.g., infinite line source, cylindrical source method, etc…). Thus, there is a need to employ modeling techniques allowing for a detailed understanding of such heat exchanges. Numerical modeling (FEM) is a suitable choice.

Finally, it can be concluded that this in situ test allows for replying to the challenge of determining the thermal characteristics of the involved materials if a correct assessment and monitoring

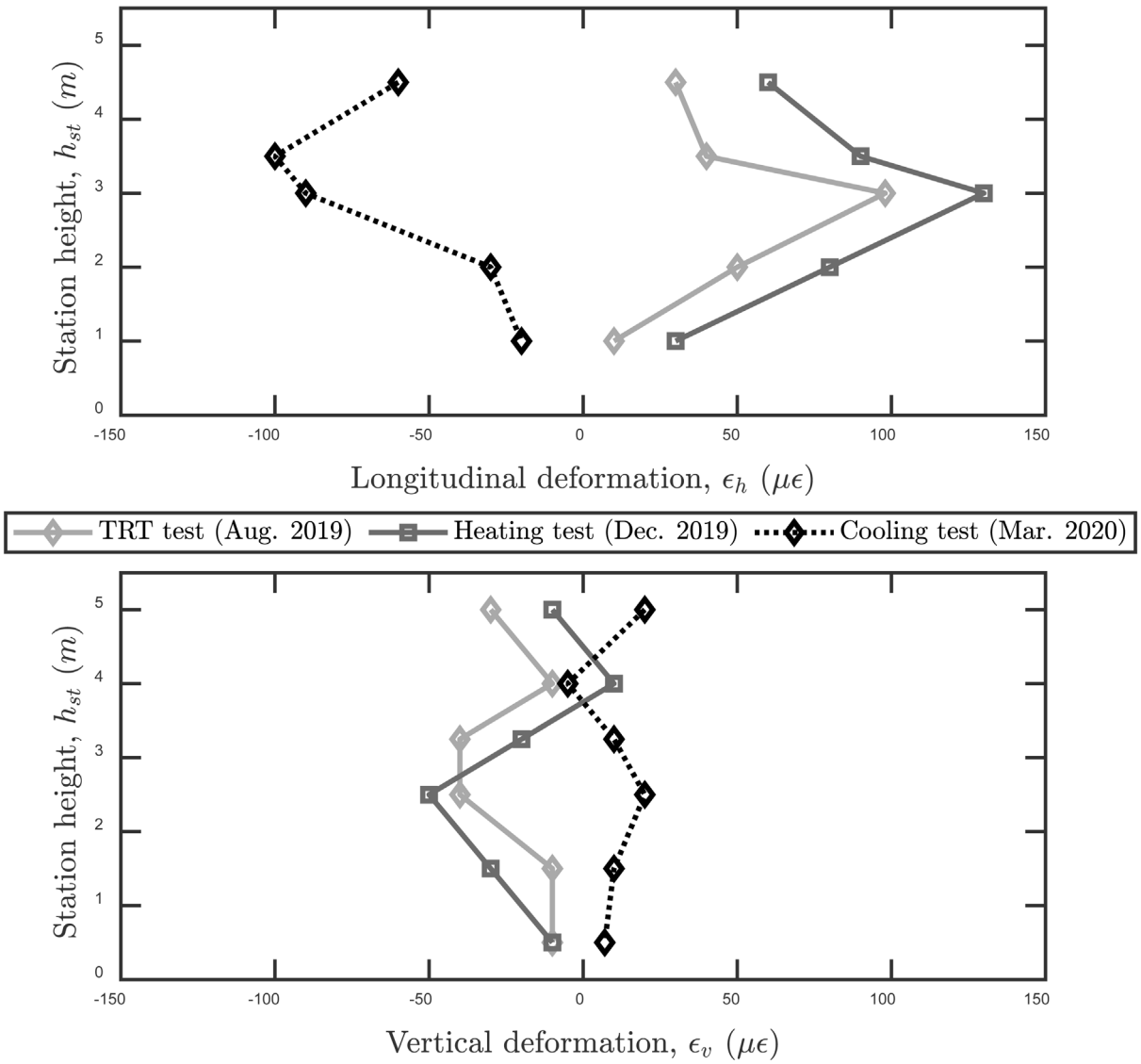

Fig. 13. Mechanical behavior of the wall intrados facing the tunnel: experimental results.

(where needed) of the relevant boundary conditions is thoroughly performed.

5. Thermomechanical behavior

The temperature variations to which the wall is subjected during heating/cooling tests induce thermomechanical effects in the geostructure. Given that the EW is in contact with different materials (i.e., concrete slabs, soil, air), different local behaviors are expected at different locations. The contact with solid materials partly constrains thermally induced deformations (i.e., low degree of freedom, *DOF*,[21,33,52,53] while at the air interface, the UEI has more freedom to deform (i.e., higher *DOF*). On the basis of the experimental and numerical results (see Appendix A for the model details), two temperature profiles in the EW are detected. At the top portion, the presence of air helps maintain a low temperature variation at the intrados. The air "washes away" the temperature difference imposed by the HEs. It follows that the EW temperature variation distribution is strongly nonuniform, with an absolute maximum located at the wall-soil interface and a minimum at the intrados. At the bottom, in the fully embedded portion, a less pronounced nonuniform temperature profile is numerically recorded as a consequence of the nonsymmetrical HE location (Fig. 12).

The monitoring system detailed in Section 2.2 is used here to evaluate the wall intrados mechanical behavior during the in situ tests. This monitoring system can record the axial deformation of the instruments, which are installed alternatively in vertical and longitudinal arrangements at the wall intrados of level -2 (Fig. 2). The results are reported in Fig. 13. The geostructure deforms when subjected to thermal loads. Deformations are partly restrained by the soil and the structural connections. The experimental results suggest that two distinct mechanisms can be identified: vertical and longitudinal mechanisms.

The temperature variation throughout the EW cross section is nonuniform (Fig. 12). Longitudinally, temperature diffuses (radially from the HEs) in the wall from the vicinity of the HE toward the intrados and toward the soil. Upon heating, the EW extrados tend to longitudinally dilate, but this dilation is partly blocked by the soil. Longitudinally, the only constraint to dilation is represented by the soil, and no wall–slab connections affect the EW behavior at any longitudinal cross section at level -2. It follows that dilation at the extrados is partly blocked, but following intrados heating, the intrados is free to dilate ($DOF_{intrados} > DOF_{extrados}$). For this reason, positive (i.e., expansion) longitudinal

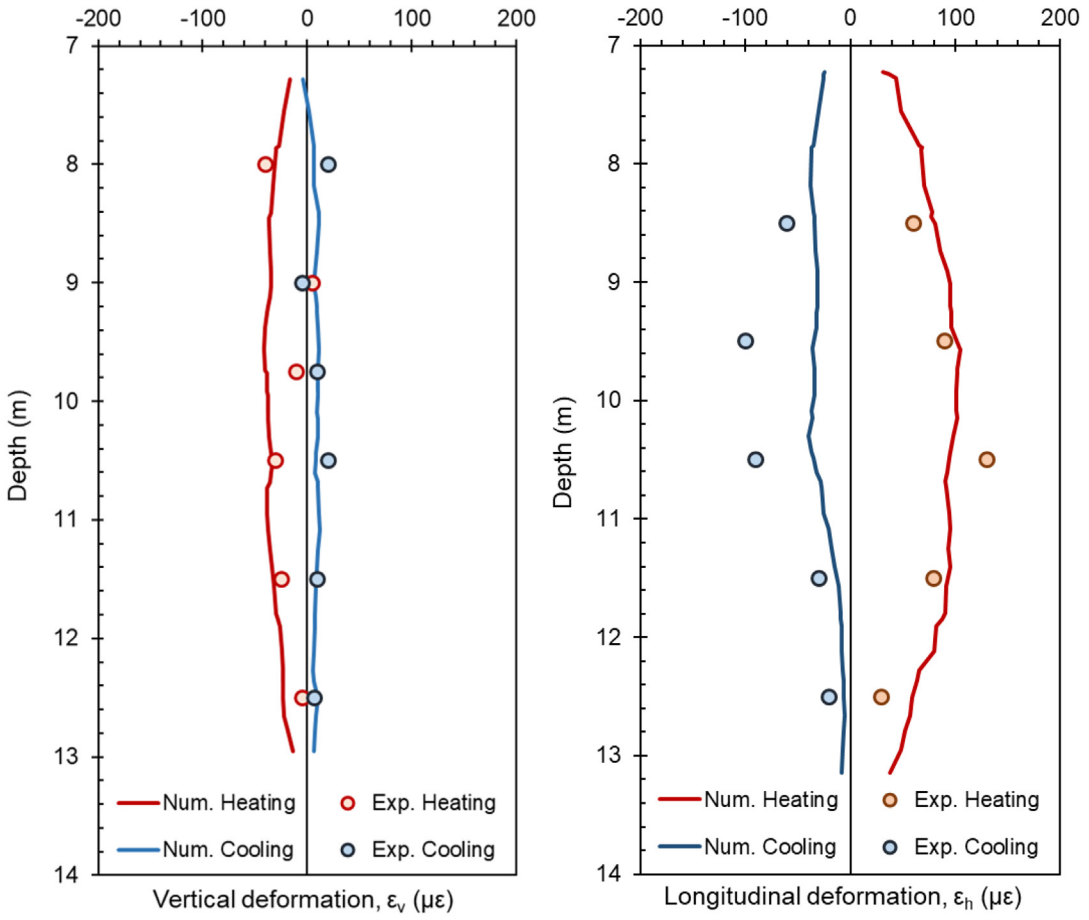

Fig. 14. Comparison of the experimental and numerical results for the heating (December 2019) and cooling (March 2020) tests.

deformation values are attained. The maximum longitudinal deformation is recorded at the tunnel mid-height, where the wall presents the lowest degree of freedom. The maximum recorded deformation value corresponds to $\varepsilon_{h,max} = \Delta L/L_0 = 0.013\%$. The deformation profile is not instantaneous, but it develops with time, in agreement with the time-dependent thermal diffusion inside the EW. The opposite was recorded upon cooling (Fig. 13).

Upon heating, the EW extrados tend to vertically dilate, but this dilation is partly blocked by the constraints (i.e., soil and structural connections). During heating tests, the extrados is hotter than the intrados (Fig. 12). Treating the EW as a vertical beam and following the hypothesis that, for small deformations, the beam cross section maintains its planarity and remains orthogonal to the neutral axis (Euler–Bernoulli theory of beams[54]), the extrados tend to vertically dilate and the intrados tend to contract (Fig. 13). Additionally, structural constraints at the top and bottom of level -2 (i.e., wall–slab connection and additional stiffness offered by the embedded portion of the wall, wall–slab connection and self-weight of the superstructure at the top) considerably restrain the degree of freedom of the wall. It follows that vertical intrados deformations are quasi-null, with a tendency of being negative (i.e., contractive) following the extrados expansion toward the soil side. The contraction is maximum at the location of the highest *DOF* at the mid-height of the wall facing the tunnel. During heating, the EW intrados vertically deforms, exhibiting a contraction. The opposite is recorded upon cooling (Fig. 13).

These results allow for a qualitative representation of the thermomechanical behavior of the EW. The experimental setup used here cannot capture a quantitative and exhaustive definition of the thermomechanical wall behavior because of constraints for the sensor's installation (i.e., a monitoring system could not be installed at the extrados). The results reported in the present study are consistent with those reported on an energy piled wall in Vienna by Brandl[9], which show maximum seasonal relative strains up to $200\mu\epsilon$, located toward the mid-height of the underground tunnel. However, limited details are available in[9] on the experimental setup, making any attempt at a more detailed comparison difficult.

To estimate the intensity of internal actions and to check the mechanical stability of the UEI, a detailed comparison accounting for thermal and mechanical load combinations is performed through 3D finite element thermohydromechanical numerical analyses. A comparison among the experimental and numerical results is first performed accounting only for thermal loads by simulating the heating and cooling tests. The results of this comparison, referring to the tunnel intrados deformations, are reported in Fig. 14 and show close agreement.

Second, a series of numerical analyses is performed, focusing on analyzing all possible ultimate (ULS) and serviceability (SLS) limit states accounting for simultaneous thermal and mechanical actions in accordance with the Swiss norm.[55–58] Along with geothermal operation and following the design details of the UEI, additional mechanical loads are included. Details are reported in Appendix B.

Fig. 15 and Fig. 16 show the results for the EW axial displacements and internal actions evaluated at the cross section in correspondence with the HEs. The vertical behavior of the EW is driven by the settlement (i.e., negative displacement) induced by applying mechanical actions. During heating, the EW partly

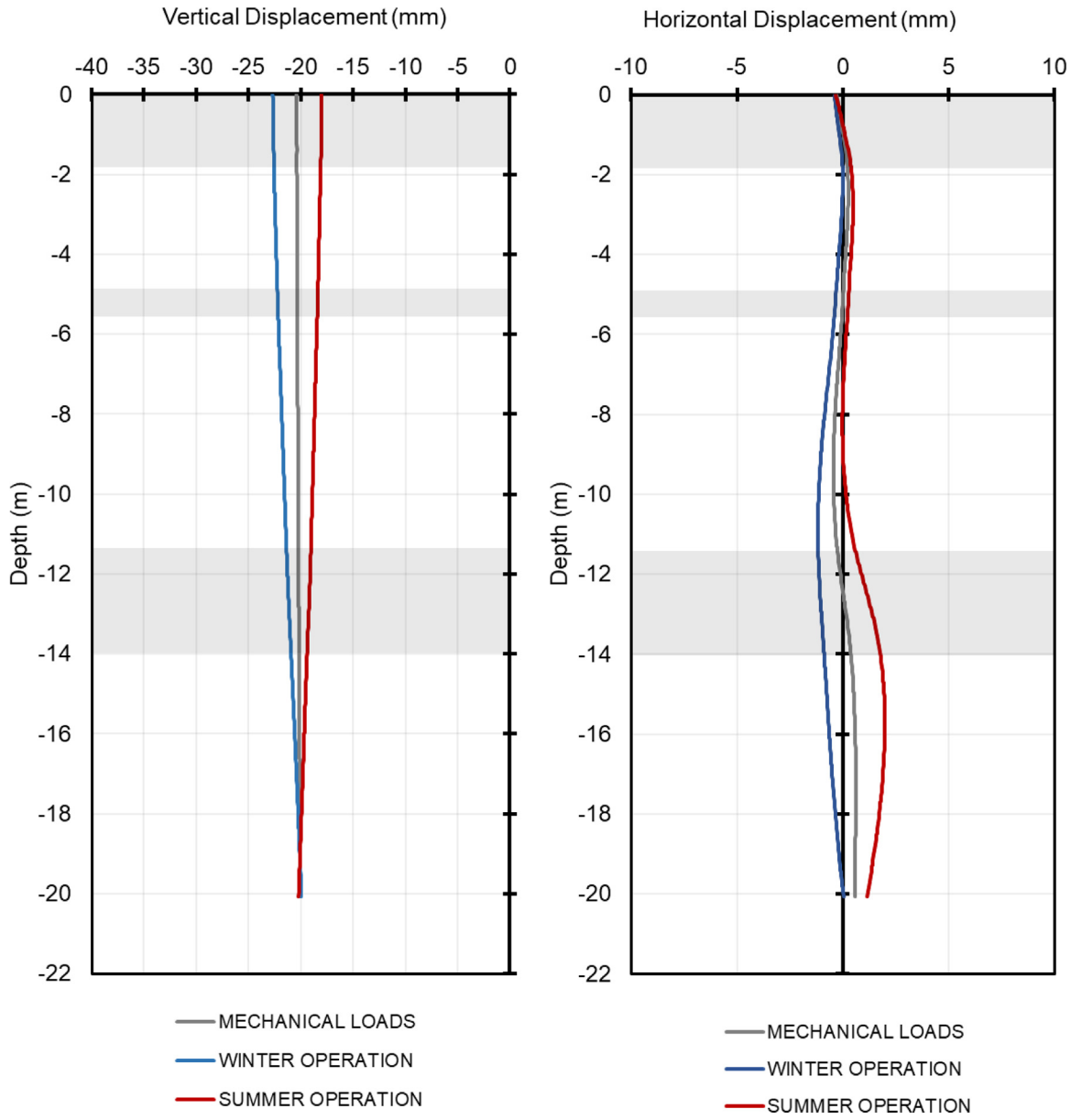

Fig. 15. Wall axis vertical and horizontal displacements at SLS: results from 3D numerical thermomechanical modeling.

expands, reducing its overall settlement. The null point[52,59] is located at the fully embedded portion near the EW toe. The opposite was recorded upon cooling. Thermal actions have a primary role in defining transversal (i.e., horizontal) displacements, consequently to the bending effects induced by the nonuniform temperature distribution. The recorded values largely respect the maximum acceptable limits defined by the Swiss norm (i.e., 20 mm for this geometry).

Internal actions follow the general behavior defined by the mechanical load application, with major variations located at the wall–slab connections due to structural stress redistribution within the structure, particularly for axial force and shear force. The bending moment shows larger discrepancies between the isothermal and nonisothermal cases. A positive bending moment (Fig. 16) upon heating means that traction develops at the intrados, while contraction develops at the extrados due to the blocked portion of thermal expansion during heating (i.e., summer operation). The opposite was recorded during cooling (i.e., winter operation). The maximum capacity of the structure (i.e., resistance bending moment, shear force, axial force) is respected.

6. Concluding remarks

This study presents the results from an experimental campaign on a full-scale underground energy infrastructure (i.e., an underground railway station) and the related numerical modeling. The main concluding remarks related to its THM behavior are summarized as follows.

The wall–tunnel hydrothermal interactions show a strong correlation between the tunnel temperature and external temperature, with high seasonal temperature variations. A relatively low speed, low scatter wind speed profile, compared with measurements on existing tunnels available in the literature,[60–66] was recorded. Low-magnitude wind speed induces low convective heat exchanges and hence low heat flux at the wall–tunnel

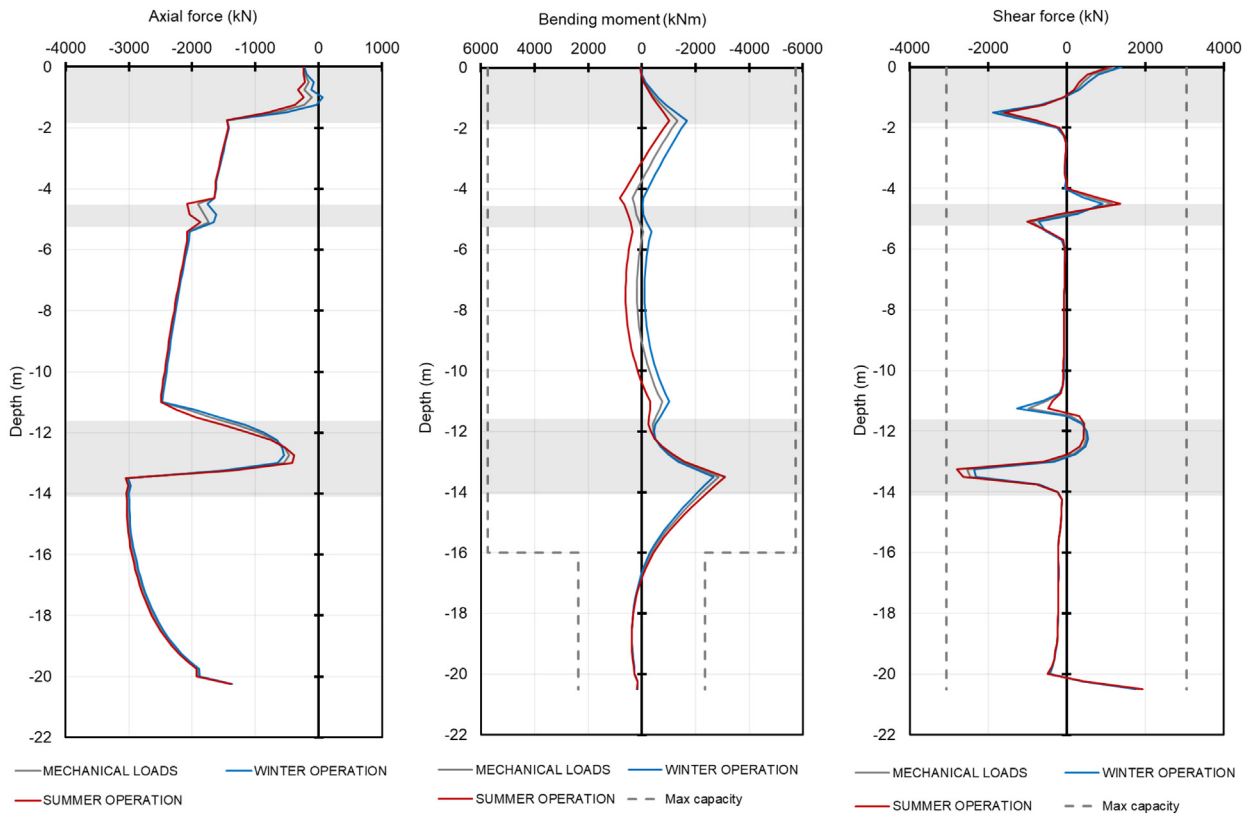

Fig. 16. Internal actions in the wall at the ULS: results from 3D numerical thermomechanical modeling.

interface. Additionally, the presence of a glass wall in the tunnel dramatically reduces the wind velocity profile near the EW, highlighting the boundary layer of the wind at the wall–tunnel interface. Thus, the tunnel, under certain circumstances, may act as a thermal resistance rather than as a conductor.

High seasonal temperature variations at the boundary conditions induce nonnegligible yearly temperature variations within the UEI. This is because the UEI is located at the thermal and hydrodynamic[1,39] entrance regions of the tunnel.

The UEI shows a very high heat storage potential (i.e., summer operation). The key aspects that highlight the heat storage potential are as follows: (*i*) the predominant heat exchange mechanism is conduction in the wall and in the soil, with absence of groundwater flow in the soil; (*ii*) the low heat flux magnitude at the wall intrados minimizes heat losses toward the tunnel, which acts as a natural insulator; and (*iii*) the high capacity of storing heat develops high HCF temperature differences between the inflow and outlet during heating tests.

During winter operation (i.e., EW cooling), the UEI has a limited operative HCF temperature range. The use of glycolyzed fluids to replace water is strongly suggested for future operations, as it would allow HCF temperatures to be reached $T_f < 0$ °C, avoiding freezing issues within the HP and surroundings and consequently increasing the thermal potential.

From a thermomechanical perspective, the UEI is very stiff. It can hence undergo high internal actions while mobilizing little displacement (i.e., high mechanical capacity). The design limits are successfully respected.

CRediT authorship contribution statement

Jacopo Zannin: Conceptualization, Methodology, Validation, Formal analysis, Investigation, Resources, Data curation, Writing – original draft, Writing – review & editing, Visualization, Project administration. **Alessio Ferrari:** Conceptualization, Validation, Resources, Writing – original draft, Writing – review & editing, Supervision, Project administration. **Tohid Kazerani:** Validation, Investigation, Resources, Project administration. **Azad Koliji:** Validation, Resources, Writing – review & editing Supervision, Project administration, Funding acquisition. **Lyesse Laloui:** Validation, Resources, Writing – review & editing, Supervision, Project administration, Funding acquisition.

Declaration of competing interest

The authors declare that they have no known competing financial interests or personal relationships that could have appeared to influence the work reported in this paper.

Acknowledgments

The authors wish to acknowledge the financial support of SIG (Services Industriels de Genève) through the project "Modélisation des géo-structures énergétiques de la gare CEVA CABA".

Appendix A. Details of the numerical model

The mathematical formulation for the finite element models used in this study is reported here. The thermo-hydro-mechanical behavior is described by the following equations. Concrete and soil are modeled as fully saturated porous materials with no groundwater flow.

The mass conservation equation of the fluid phase in the porous media reads:

$$\frac{\partial}{\partial t}(n\rho_w) + \operatorname{div}(\rho_w \boldsymbol{v_{rw}}) = 0 \tag{A.1}$$

where n is the porosity of the porous medium, ρ_w is the fluid density, t is the time, and $\boldsymbol{v_{rw}} = 0$ is the fluid velocity according to Darcy's law.

The energy conservation equation can be separated into two parts: one that relates to the conductive and convective heat transfer processes in the porous materials and another to the hydrothermal fluid flow inside the heat exchangers.

The former part can be written as

$$\operatorname{div}(\lambda\, \mathbf{grad} T) = \rho C_p \frac{\partial T}{\partial t} + \rho_w C_{p,w} \boldsymbol{v_{rw}} \cdot \mathbf{grad} T \tag{A.2}$$

in which λ is the thermal conductivity of the effective material:

$$\lambda = (1-n)\,\lambda_s + n\lambda_w \tag{A.3}$$

where the subscripts s and w relate to the solid and fluid phases, respectively. T is the temperature, and ρC_p is the effective volumetric heat capacity at constant pressure:

$$\rho C_p = (1-n)\,\rho_s C_{p,s} + n\rho_w C_{p,w} \tag{A.4}$$

The second part of the energy conservation equation relating to the nonisothermal fluid flow inside the heat exchangers accounts for the convective heat exchanges within the fluid and for conduction through the pipe wall:

$$\rho_f c_f A_p \frac{\partial T_{bulk,f}}{\partial t} + \rho_f c_f A_p \boldsymbol{u_f} \cdot \mathbf{grad}\left(T_{bulk,f}\right) = \operatorname{div}\left[A_p \lambda_f \mathbf{grad}\left(T_{bulk,f}\right)\right] + \dot{q}_p \tag{A.5}$$

where ρ_f, c_f, $T_{bulk,f}$, $\boldsymbol{u_f}$, λ_f are the bulk density, specific heat at constant pressure, bulk temperature, tangential velocity and thermal conductivity of the fluid, respectively. The cross section of the heat exchanger pipe is A_p, and $\dot{q}_p$ expresses the heat flux per unit length through the pipe wall, which is defined as:

$$\dot{q}_p = U P_p \left(T_{ext} - T_{bulk,f}\right) \tag{A.6}$$

where U relates to an effective value of the pipe heat transfer coefficient accounting for the thermal resistances of the internal film and the wall. U is expressed as a function of the hydraulic radius, pipe geometry and thermal conductivity of the pipe material. $P_p = 2\pi r_{int}$ is the wetted perimeter of the pipe cross section, and T_{ext} is the external temperature of the pipe.[30,34,67–69]

The equilibrium equation reads as:

$$\operatorname{div}\boldsymbol{\sigma} + \rho \mathbf{g} = 0 \tag{A.7}$$

where div denotes the divergence operator, $\boldsymbol{\sigma}$ is the total stress tensor, ρ is the density of the porous material, and $\boldsymbol{g}$ is the gravity vector. In the framework of thermo-elasticity, when drained conditions are considered (*i.e.*, variations in total stress are equivalent to variations in effective stress), the constitutive law reads:

$$\mathrm{d}\boldsymbol{\sigma} = \mathbf{C}\,(d\boldsymbol{\varepsilon} + \boldsymbol{\beta} dT) \tag{A.8}$$

where $\boldsymbol{C}$ is the constitutive tensor, $\boldsymbol{\varepsilon}$ is the total strain tensor, $\boldsymbol{\beta}$ is a tensor that contains the thermal expansion coefficient (α) in the main diagonal, and T is the temperature.

With reference to the model geometry presented in Fig. 8, the external mechanical loads detailed in Appendix B are applied as surface loads. The results from piezometric readings (dated to 2008) at a location approximately 150 m from the considered cross section (i.e., Fig. 1) suggest that the groundwater table is located in the gravel layer. The following hydraulic boundaries are set: for SLS calculations, the groundwater table is considered at the top of layer D (Fig. 1, Table 1) and under hydrostatic conditions; hence, negative pore water pressures develop above the groundwater table, and the materials are considered saturated (saturated unit weight, γ_{sat}); for ULS calculations, an additional case is defined, aiming at defining a worst-case scenario, which foresees the groundwater table located at the top of layer B (i.e., at the top of the geostructure) and under hydrostatic conditions. Under these conditions, layers B, C and D are below the groundwater table (i.e., characterized by their submerged unit weight, γ'). These two conditions are used in the definition of the combinations of actions together with the thermal and mechanical loads reported in Appendix B.

First, the model is hydromechanically initialized at rest (K_0) conditions and at a uniform temperature $T_s = 14.5$ °C. This assumption is a simplification of reality. No details and monitoring during the construction processes are available, making completely arbitrary, at this stage, any attempt to consider thermomechanical aspects during the construction process, which occurred more than 5 years before the execution of the first thermal tests (i.e., the TRT in August 2019). Additionally, the geostructural response following the hypothesis of elasticity of all materials (Fig. 14) seems to give a satisfactory representation of reality.

Second, a transient analysis is performed. In addition to the hydromechanical description reported at the first step, thermal boundary conditions (reported in Section 4.1) are simulated for 10 years to ensure a periodical response independent of the initial conditions.

Third, thermomechanical loads are applied. They involve the concurrent application of the thermal input induced by geothermal operation for winter and summer, together with the combinations of mechanical loads taken following the Swiss norms (Appendix B).

Appendix B. Rationale for applying mechanical loads

This appendix expands on the additional thermomechanical loads accounted for during the analyses reported in Section 5. In conjunction with thermal operation, the following mechanical

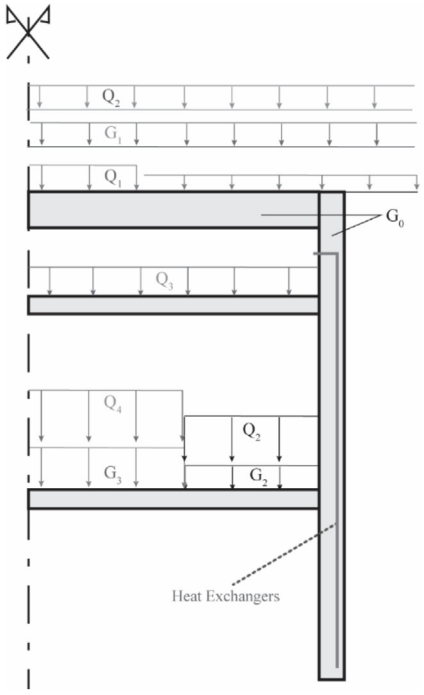

Fig. 17. Sketch of the geostructural geometry over a vertical cross section corresponding to the heat exchangers with indications of the mechanical loads detailed in.

Table B.1
Description of the mechanical loads considered for the thermomechanical analysis.

Name	Description	Characteristic value	Unit
Dead loads			
G_0	Structure unit weight	25.0	kN/m^3
G_1	Embankment surcharge	56.0	kN/m^2
G_2	Structural surcharge	40.0	kN/m^2
G_3	Rail ballast	22.0	kN/m^2
Live loads			
Q_1	Road traffic (tramway)	26.6	kN/m^2
		2.3	kN/m^2
Q_2	Pedestrian load	4.0	kN/m^2
Q_3	Crowding surcharge	10.0	kN/m^2
Q_4	Train load	92.4	kN/m^2

loads are considered: train load, ballast load and structural surcharges at level -2, crowding load at level -1, road traffic, embankment and pedestrian surcharges at level 0 (Fig. 17 and Table B.1). Following the Swiss norm, the following load combinations for the ULS (Eq. (B.1)) and SLS (Eq. (B.2)) are considered:

$$1.35 \sum_i G_i + 1.5 \left(\sum_i Q_i + q_T T \right) \tag{B.1}$$

$$\sum_i G_i + \sum_i Q_i + q_T T \tag{B.2}$$

$$\sum_i G_i + 0.6 \sum_i Q_i + T$$

where G_i and Q_i are detailed in Table B.1, and T represents the yearly profile of heat carrier fluid temperature imposed at the inflow point (i.e., 6 months of heating followed by 6 months of cooling). $q_T = 0.6$ represents a nondimensional multiplier from the Swiss norm.

References

1. Laloui L, Rotta Loria AF. *Analysis and Design of Energy Geostructures - 1st Edition*. Academic Press; 2019.
2. Sutman M, Speranza G, Ferrari A, Larrey-Lassalle P, Laloui L. Long-term performance and life cycle assessment of energy piles in three different climatic conditions. *Renew Energy*. 2020;146:1177–1191. http://dx.doi.org/10.1016/j.renene.2019.07.035.
3. Brandl H. Energy foundations and other thermo-active ground structures. *Géotechnique*. 2006;56:81–122. http://dx.doi.org/10.1680/geot.2006.56.2.81.
4. Xia C, Sun M, Zhang G, Xiao S, Zou Y. Experimental study on geothermal heat exchangers buried in diaphragm walls. *Energy Build*. 2012;52:50–55. http://dx.doi.org/10.1016/j.enbuild.2012.03.054.
5. Nicholson DP, Chen Q, de Silva M, Winter A, Winterling R. The design of thermal tunnel energy segments for Crossrail, UK. *Proc Inst Civ Eng - Eng Sustain*. 2014;167:118–134. http://dx.doi.org/10.1680/ensu.13.00014.
6. Makasis N, Narsilio GA, Bidarmaghz A, Johnston IW, Zhong Y. The importance of boundary conditions on the modelling of energy retaining walls. *Comput Geotech*. 2020;120:103399. http://dx.doi.org/10.1016/j.compgeo.2019.103399.
7. Sterpi D, Angelotti A, Habibzadeh-Bigdarvish O, Jalili D. Assessment of thermal behaviour of thermo-active diaphragm walls based on monitoring data. *J Rock Mech Geotech Eng*. 2018;10:1145–1153. http://dx.doi.org/10.1016/j.jrmge.2018.08.002.
8. Sterpi D, Tomaselli G, Angelotti A. Energy performance of ground heat exchangers embedded in diaphragm walls: Field observations and optimization by numerical modelling. *Renew Energy Shallow Geothermal Energy Systems*. 2020;147:2748–2760. http://dx.doi.org/10.1016/j.renene.2018.11.102.
9. Brandl H. Geothermal geotechnics for urban undergrounds. In: *Procedia Eng., 15th International Scientific Conference "Underground Urbanisation As a Prerequisite for Sustainable Development" 12–15 Septembe 2016, St. Petersburg, Russia. Vol. 165*. 2016:747–764. http://dx.doi.org/10.1016/j.proeng.2016.11.773.
10. Loveridge F, McCartney JS, Narsilio GA, Sanchez M. Energy geostructures: A review of analysis approaches, in situ testing and model scale experiments. *Geomech Energy Environ*. 2020;22:100173. http://dx.doi.org/10.1016/j.gete.2019.100173.
11. Makasis N, Narsilio GA. Energy diaphragm wall thermal design: The effects of pipe configuration and spacing. *Renew Energy*. 2020;154:476–487. http://dx.doi.org/10.1016/j.renene.2020.02.112.
12. Shafagh I, Rees S, Urra Mardaras I, Curto Janó M, Polo Carbayo M. A model of a diaphragm wall ground heat exchanger. *Energies*. 2020;13:300. http://dx.doi.org/10.3390/en13020300.
13. Bowles JE. *Foundation Analysis and Design*. 4th ed. USA: McGraw-Hill Book Company. ed.; 1988.
14. Lambe TW, Whitman RV. *Soil Mechanics*. John Wiley & Sons; 1991.
15. GSHPA. Thermal piles standard. 2012.
16. Mattsson N, Steinmann G, Laloui L. Advanced compact device for the in situ determination of geothermal characteristics of soils. *Energy Build*. 2008;40:1344–1352. http://dx.doi.org/10.1016/j.enbuild.2007.12.003.
17. Gehlin S, Hellström G. Recent status of in-situ thermal response tests for BTES applications in Sweden. *Proc Terrastock*. 2000;2000:159–164.
18. Gehlin S. Thermal response test: method development and evaluation. 2002.
19. Laloui L, Nuth M, Vulliet L. Experimental and numerical investigations of the behaviour of a heat exchanger pile. *Int J Numer Anal Methods Geomech*. 2006;30:763–781. http://dx.doi.org/10.1002/nag.499.
20. Sanner B, Hellström G, Spitler J, Gehlin S. Thermal response test–current status and world-wide application. In: *Proceedings World Geothermal Congress*. International Geothermal Association; 2005:24–29.
21. Zannin J. *Thermomechanical Behavior of Underground Energy Infrastructures* [Ph.D. thesis nr. 8450]. Swiss Federal Institute of Technology in Lausanne, EPFL; 2020.
22. Pahud D, Matthey B. Comparison of the thermal performance of double U-pipe borehole heat exchangers measured in situ. *Energy Build*. 2001;33:503–507. http://dx.doi.org/10.1016/S0378-7788(00)00106-7, Special Issue: Proceedings of the International Conference on.
23. Rotta Loria AF, Laloui L. Thermally induced group effects among energy piles. *Géotechnique*. 2017;67:374–393. http://dx.doi.org/10.1680/jgeot.16.P.039.
24. Gao L, Zhao J, Tang Z. A review on borehole seasonal solar thermal energy storage. *Energy Procedia*. 2015;70:209–218.
25. Gehlin S. 11 - Borehole thermal energy storage. In: Rees SJ, ed. *Advances in Ground-Source Heat Pump Systems*. Woodhead Publishing; 2016:295–327. http://dx.doi.org/10.1016/B978-0-08-100311-4.00011-X.
26. Nordell B, Andersson O, Rydell L, Scorpo AL. Long-term performance of the HT-BTES in Emmaboda, Sweden. In: *Presented at the Greenstock 2015: International Conference on Underground Thermal Energy Storage 19/05/2015-21/05/2015*. 2015.
27. Reuss M. 6 - The use of borehole thermal energy storage (BTES) systems. In: Cabeza LF, ed. *Advances in Thermal Energy Storage Systems*. Woodhead Publishing; 2015:17–147. In: Woodhead Publishing Series in Energy; http://dx.doi.org/10.1533/9781782420965.1.117.
28. Witte HJL, Van Gelder AJ. Three years monitoring of a borehole thermal energy store of a UK office building. In: Paksoy HÖ, ed. *Thermal Energy Storage for Sustainable Energy Consumption*. Dordrecht: Springer Netherlands; 2007:205–219. In: NATO Science Series; http://dx.doi.org/10.1007/978-1-4020-5290-3_11.
29. Adam D, Markiewicz R. Energy from earth-coupled structures, foundations, tunnels and sewers. *Géotechnique*. 2009;59:229–236. http://dx.doi.org/10.1680/geot.2009.59.3.229.
30. Batini N, Rotta Loria AF, Conti P, Testi D, Grassi W, Laloui L. Energy and geotechnical behaviour of energy piles for different design solutions. *Appl Therm Eng*. 2015;86:199–213. http://dx.doi.org/10.1016/j.applthermaleng.2015.04.050.
31. Di Donna A. Energy walls for an underground car park. In: *25th Eur. Young Geotech. Eng. Conf*. 2016:21–24.
32. Kavanaugh SP, Rafferty KD. *Geothermal Heating and Cooling: Design of Ground-Source Heat Pump Systems*. Atlanta: ASHRAE. ed.; 2014.
33. Zannin J, Rotta Loria AF, Llabjani Q, Laloui L. Extension of Winkler's solution to non-isothermal conditions for capturing the behaviour of plane geostructures subjected to thermal and mechanical actions. *Comput. Geotech*. 2020.
34. COMSOL Inc. *COMSOL Multiphysics Reference Manual, Version 5.3*. 2018 www.comsol.com.
35. Bourne-Webb P, Burlon S, Javed S, Kürten S, Loveridge F. Analysis and design methods for energy geostructures. *Renew Sustain Energy Rev*. 2016;65:402–419. http://dx.doi.org/10.1016/j.rser.2016.06.046.
36. Bourne-Webb PJ, Bodas Freitas TM, da Costa Gonçalves RA. Thermal and mechanical aspects of the response of embedded retaining walls used as shallow geothermal heat exchangers. *Energy Build*. 2016;125:130–141. http://dx.doi.org/10.1016/j.enbuild.2016.04.075.
37. Guo Lixia, Guo Lei, Zhong L, Zhu Y. Thermal conductivity and heat transfer coefficient of concrete. *J Wuhan Univ Technol-Mater Sci Ed*. 2011;26:791–796. http://dx.doi.org/10.1007/s11595-011-0312-3.

38. Lee Y, Choi M-S, Yi S-T, Kim J-K. Experimental study on the convective heat transfer coefficient of early-age concrete. *Cem Concr Compos*. 2009;31:60–71. http://dx.doi.org/10.1016/j.cemconcomp.2008.09.009.
39. Peltier M, Rotta Loria AF, Lepage L, Garin E, Laloui L. Numerical investigation of the convection heat transfer driven by airflows in underground tunnels. *Appl Therm Eng*. 2019;159:113844. http://dx.doi.org/10.1016/j.applthermaleng.2019.113844.
40. Loveridge Fa, Olgun Cg, Brettmann T, Powrie W. Group thermal response testing for energy piles. In: *Geotechnical Engineering for Infrastructure and Development, Conference Proceedings*. ICE Publishing; 2015:2595–2600. http://dx.doi.org/10.1680/ecsmge.60678.vol5.400.
41. Zannin J, Ferrari A, Pousse M, Laloui L. Thermal design and full-scale thermal response test on energy walls. *E3S Web Conf*. 2019;92(18011). http://dx.doi.org/10.1051/e3sconf/20199218011.
42. Asadi I, Shafigh P, Abu Hassan ZFB, Mahyuddin NB. Thermal conductivity of concrete – A review. *J Build Eng*. 2018;20:81–93. http://dx.doi.org/10.1016/j.jobe.2018.07.002.
43. Valore R. Calculations of U-values of hollow concrete masonry. *Concr Int*. 1980;2:40–63.
44. Zhang W, Min H, Gu X, Xi Y, Xing Y. Mesoscale model for thermal conductivity of concrete. *Constr Build Mater*. 2015;98:8–16. http://dx.doi.org/10.1016/j.conbuildmat.2015.08.106.
45. Vulliet L, Laloui L, Zhao J. *Mécanique des sols et des roches (TGC volume 18): avec écoulements souterrains et transferts de chaleur*. PPUR Presses polytechniques; 2016.
46. CFMS-SYNTEC-SOFFONS-FNTP. Recommandations pour la conception, le dimensionnement et la mise en oeuvre des géostructures thermiques. 2017:120.
47. SIA D0190. Utilisation de la Chaleur du Sol par des Ouvrages de Fondation et de Soutènement en Béton. Guide pour la Conception, la Realisation et la Maintenance. 2005.
48. Mimouni T, Laloui L. Behaviour of a group of energy piles. *Can Geotech J*. 2015;52:1913–1929. http://dx.doi.org/10.1139/cgj-2014-0403.
49. Rotta Loria AF, Laloui L. Group action effects caused by various operating energy piles. *Géotechnique*. 2017;68:834–841. http://dx.doi.org/10.1680/jgeot.17.P.213.
50. Di Donna A, Barla M, Amis T. Energy Geostructures: Analysis from research and systems installed around the World. In: *DFI 42nd Annual Conference on Deep Foundations. New Orleans, United States*. 2017.
51. Carslaw HS, Jaeger JC. *Conduction of heat in solids*. Clarendon Press; 1952.
52. Rotta Loria AF, Bocco M, Garbellini C, Muttoni A, Laloui L. The role of thermal loads in the performance-based design of energy piles. *Geomech Energy Environ*. 2020;21:100153. http://dx.doi.org/10.1016/j.gete.2019.100153.
53. Loria AFR, Zannin J, Llabjani Q, Laloui L. Analytical solution for describing the thermo-mechanical behavior of plane energy geostructures. *E3S Web Conf*. 2020;205:06009. http://dx.doi.org/10.1051/e3sconf/202020506009.
54. Truesdell C. The rational mechanics of flexible or elastic bodies 1638–1788. In: *Leonhardi Euleri Opera Omnia, Turici*. Zürich: Venditioni exponunt Orell Füssli(IS). ed, 2; 1960.
55. SIA 197/1. *Projets de Tunnels, Tunnels Ferroviaires*. Zurich: Société suisse des ingénieurs et des architectes; 2004.
56. SIA 261 and 261/1. *Actions sur Les Structures Porteuses Et Actions sur Les Structures Porteuses – Spécifications Complémentaires*. Zurich: Société suisse des ingénieurs et des architectes; 2003.
57. SIA 262. *Construction en Béton*. Zurich: Société suisse des ingénieurs et des architectes; 2003.
58. SIA 267 and 267/1. *Géotechnique et Géotechnique –Spécifications Complémentaires*. Zurich: Société suisse des ingénieurs et des architectes; 2003.
59. Laloui L, Di Donna A. *Energy Geostructures: Innovation in Underground Engineering*. Hoboken, NJ, USA: ISTE and John Wiley & Sons. ed.; 2013.
60. He X, Li A, Ning Y. Optimization of outdoor design temperature for summer ventilation for undersea road tunnel using field measurement and statistics. *Build Environ*. 2020;167:106457. http://dx.doi.org/10.1016/j.buildenv.2019.106457.
61. Jin S, Jin J, Gong Y. A theoretical explanation of natural ventilation at roof openings in urban road tunnels. *Tunn Undergr Space Technol*. 2020;98:103345. http://dx.doi.org/10.1016/j.tust.2020.103345.
62. Pflitsch A, Bruene M, Steiling B, et al. Air flow measurements in the underground section of a UK light rail system. *Appl Therm Eng*. 2012;32:22–30. http://dx.doi.org/10.1016/j.applthermaleng.2011.07.030.
63. Pflitsch A, Kuesel H. Subway-climatology–new research field for the management of possible catastrophes in subway systems. In: *Man Clim. 20th Century Stud. Geogr. 75*. 2003:384–394.
64. Steinemann U, Zumsteg F, Wildi P. Measurements of air flow, temperature differences and pressure differences in road tunnels. In: *Int. Conf. Tunn. Saf. Vent. Graz Austria*. 2004:220–226.
65. Woods WA, Pope CW. A generalised flow prediction method for the unsteady flow generated by a train in a single-track tunnel. *J Wind Eng Ind Aerodyn*. 1981;7:331–360. http://dx.doi.org/10.1016/0167-6105(81)90057-X.
66. Zhao P, Chen J, Luo Y, et al. Field measurement of air temperature in a cold region tunnel in northeast China. *Cold Reg Sci Technol*. 2020;171:102957. http://dx.doi.org/10.1016/j.coldregions.2019.102957.
67. Gnielinski V. New equations for heat and mass transfer in turbulent pipe and channel flow. *Int Chem Eng*. 1976;16:359–368.
68. Haaland SE. Simple and explicit formulas for the friction factor in turbulent pipe flow. *J Fluids Eng*. 1983;105:89–90. http://dx.doi.org/10.1115/1.3240948.
69. Zannin J, Ferrari A, Pousse M, Laloui L. Hydrothermal interactions in energy walls. *Undergr Space*. 2020. http://dx.doi.org/10.1016/j.undsp.2020.02.001.